Earthquakes and Structures, *Vol. 5, No. 2 (2013) 161-205*
DOI: http://dx.doi.org/10.12989/eas.2013.5.2.161

Seismic motions in a non-homogeneous soil deposit with tunnels by a hybrid computational technique

G.D. Manolis[*1], Konstantia Makra[2], Petia S. Dineva[3] and Tsviatko V. Rangelov[4]

[1]*Department of Civil Engineering, Aristotle University, 54124 Thessaloniki, Greece*
[2]*Institute of Engineering Seismology and Earthquake Engineering, P.O. Box 53, 55102 Thessaloniki, Greece*
[3]*Institute of Mechanics, Bulgarian Academy of Sciences, 1113 Sofia, Bulgaria*
[4]*Institute of Mathematics and Informatics, Bulgarian Academy of Sciences, 1113 Sofia, Bulgaria*

(Received July 3, 2012, Revised January 18, 2013, Accepted February 5, 2013)

Abstract. We study seismically induced, anti-plane strain wave motion in a non-homogeneous geological region containing tunnels. Two different scenarios are considered: (a) The first models two tunnels in a finite geological region embedded within a laterally inhomogeneous, layered geological profile containing a seismic source. For this case, labelled as the first boundary-value problem (BVP 1), an efficient hybrid technique comprising the finite difference method (FDM) and the boundary element method (BEM) is developed and applied. Since the later method is based on the frequency-dependent fundamental solution of elastodynamics, the hybrid technique is defined in the frequency domain. Then, an inverse fast Fourier transformation (FFT) is used to recover time histories; (b) The second models a finite region with two tunnels, is embedded in a homogeneous half-plane, and is subjected to incident, time-harmonic SH-waves. This case, labelled as the second boundary-value problem (BVP 2), considers complex soil properties such as anisotropy, continuous inhomogeneity and poroelasticity. The computational approach is now the BEM alone, since solution of the surrounding half plane by the FDM is unnecessary. In sum, the hybrid FDM-BEM technique is able to quantify dependence of the signals that develop at the free surface to the following key parameters: seismic source properties and heterogeneous structure of the wave path (the FDM component) and near-surface geological deposits containing discontinuities in the form of tunnels (the BEM component). Finally, the hybrid technique is used for evaluating the seismic wave field that develops within a key geological cross-section of the Metro construction project in Thessaloniki, Greece, which includes the important Roman-era historical monument of Rotunda dating from the 3rd century A.D.

Keywords: SH-waves; anisotropy; inhomogeneity; poroelasticity; tunnels; local site effects; seismic response; hybrid FDM-BEM

1. Introduction

A BEM formulation based on a new type of fundamental solution derived by the Radon transform (Rangelov *et al*. 2005) is interfaced with the FDM (Moczo *et al*. 2007) and used to synthesize seismic signals in complex geological regions for design purposes. The particular soil deposit considered herein is a cross-section containing two underground Metro tunnels in the

[*]Corresponding author, Professor, E-mail: gdm@civil.auth.gr

http://www.techno-press.org/?journal=eas&subpage=7 ISSN: 2092-7614 (Print), 2092-7622 (Online)

centre of the town of Thessaloniki, Greece, a short distance from an important Roman monument complex known as the Rotunda (see Fig.1 for the general setting). Fig. 2 depicts a larger 2D, north-south cross-section reaching to the sea (modelled by the FDM), while Fig. 3 shows the immediate area (modelled by the BEM) surrounding the two Metro tunnels and including the Rotunda.

It becomes obvious that the local soil material profile exhibiting inhomogeneity, anisotropy and poroelasticity plays an important role for site effects, since we are dealing with debris-type deposits in an urban centre accumulating for over two millennia. Obviously, the seismic wave fields that develop at the free surface are the result of a complex interplay of geometric and material factors, even for the simple model of SH-wave propagation, and cannot be estimated without recourse to numerical modelling techniques (Raptakis *et al.* 2004a, 2004b, Moczo and Bard 1993, Smerzini *et al.* 2009, Goto *et al.* 2010).

(a)

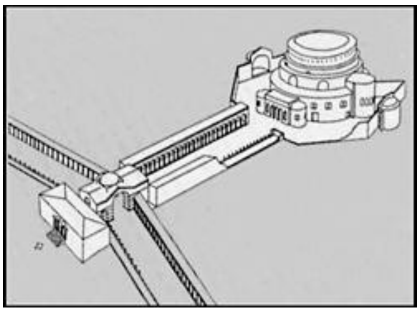

(b)

(c)

Fig. 1 (a) The Thessaloniki, Greece, Metro line (9 km under construction) with the 'Syntrivani' Metro station area; (b) the 'Syntrivani' Metro station area with a reconstruction of the Roman-era Rotunda monument complex and (c) the Arch of Galerius as it appears today

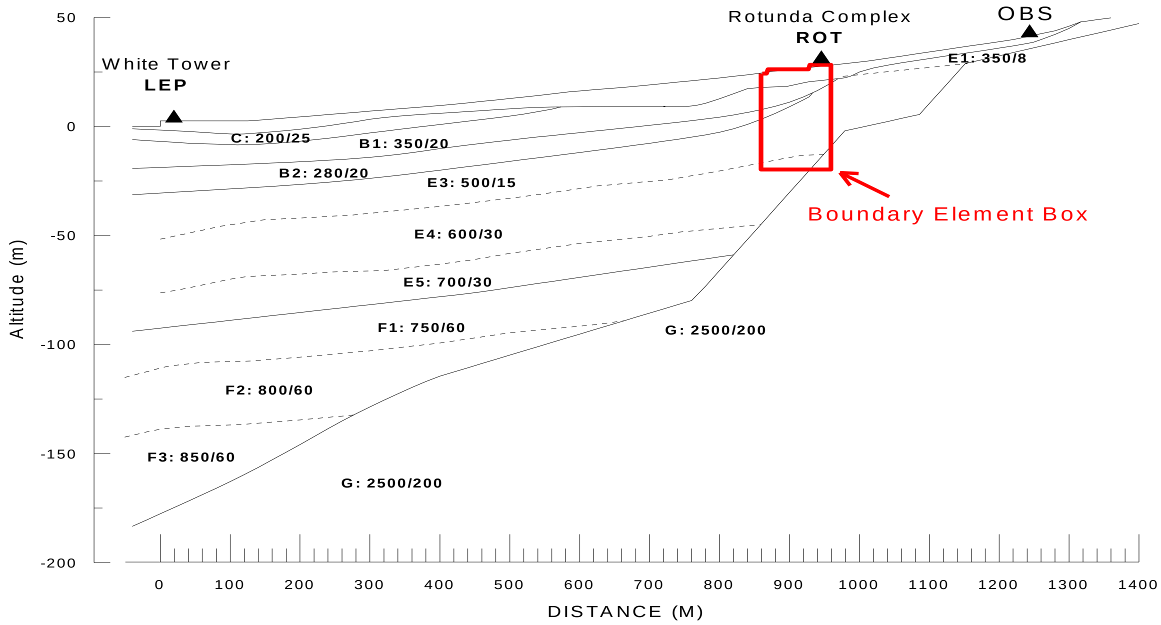

Fig. 2 Two dimensional, N-S cross-section through the 'Syntrivani' Metro station area from the hills directly above (OBS) through the Rotunda monument complex (ROT) and to the White Tower monument (LEP) by the sea, depicting the 'BEM box' and the local soil stratigraphy with mean shear wave *Vs (m/s)* and quality factor *Q* values for the main soil formations *A-G* (after Raptakis *et al.* 2004a)

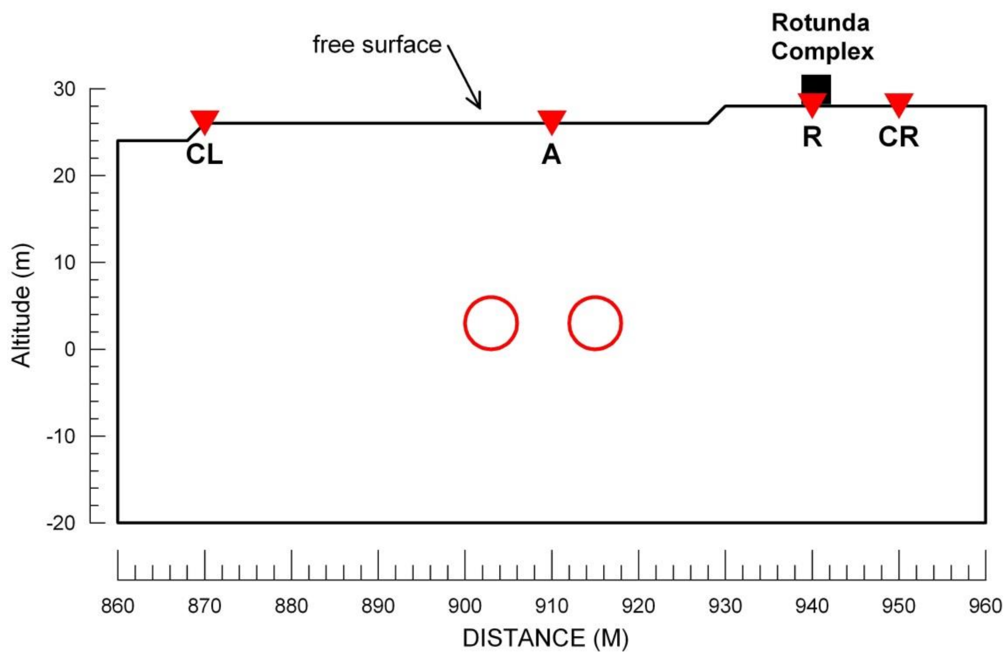

Fig. 3 2D cross-section of the immediate Syntrivani Metro station area with the two buried Metro tunnels and the Rotunda monument complex showing four observation points

A considerable amount of work has been reported in the literature on the mathematical modelling, quantification and ultimate prediction of site response in the event of an earthquake. It remains impossible, however, to have an accurate evaluation of the seismic response at a given location for future earthquakes without a detailed description of site effects. More specifically, earthquakes are triggered from a source mechanism that releases energy in the form of seismic waves. These waves filter through geological media on their way to the free surface and are greatly affected by the material properties and structure of the soil layers, including local topography. As result, the spatial and temporal variation of seismic signals differs considerably for nearby stations in the same locality and even for the same earthquake (EERI 2003). On the other hand, seismic design codes (CEN 2004) allude to the importance of site effects by focusing on a detailed categorization of the local soil deposits. To date, it has been proven diffcult to incorporate site effects in seismic design codes because of the sheer complexity of the problem. This partially reflects in the relative paucity of numerical models capable of handling irregular site geometry and complex soil deposits. In order to place the problem in its proper perspective, a brief review of the literature on the influence of soil properties (e.g., anisotropy, poroelasticity, inhomogeneity) on the local seismic wave field is given below. We focus on numerical techniques and primarily on the BEM (Dineva and Manolis 2001, Alvarez-Rubio *et al.* 2005, Luzon *et al.* 2002, Gatmiri *et al.* 2009, Wuttke *et al.* 2011, Buchon and Sanchez-Sesma 2007), which appears to be suitable for investigating the effect of local site conditions and the repercussions this has on the development of free surface wave fields. More specifically, the BEM is an attractive candidate for modelling wave motion in non-homogeneous geological deposits because of certain advantages, namely: (a) the integral equation formulation used is equivalent to the original governing equations and boundary conditions. This fact, coupled with the use of fundamental solutions for these governing equations, guarantees a high level of accuracy; (b) these same fundamental solutions obey the Sommerfeld radiation condition and thus infinitely extended boundaries are automatically accounted for without resorting to special types of viscous boundaries; (c) since only surfaces need to modelled, there is reduction of the problem dimensionality, with a corresponding reduction in the size of the system matrices as compared with domain-type numerical methods; (d) selective solution at internal points in the domain of interest is possible once the BVP has been solved, which obviates the large scale volume discretization previously mentioned; (e) flexibility in modelling surface relief, in contrast to semi-analytical methods and to the FDM, see Moczo *et al.* 1997; (f) concurrent recovery of both displacements and tractions at a comparable accuracy level.

1.1 Seismic wave propagation in anisotropic media

Following fundamental work on anisotropic elasticity (Lekhnitskii 1963), BEM formulations were first presented in Rizzo and Shippy (1970) and Snyder and Cruse (1975). The difficulty with such formulations stems from the complexity in deriving fundamental solutions for anisotropy, especially in the case of dynamic problems. These solutions are in integral form, with the integration path defined either over a finite domain (Wang and Achenbach 1995) or an infinite one (Dravinski and Niu 2002). In terms of application examples, Saez and Domınguez (1999) used the conventional BEM formulation for wave diffraction problems in 3D transversally isotropic solids. Alternative BEM formulations were applied to wave diffraction in 2D anisotropic solids by Kobayashi *et al*. (1986) and Wang *et al*. (1996). Also, Ahmad *et al*. (2001) presented a BEM formulation based on Green’s functions in the form of infinite integrals for the analysis of dynamic soil-structure-interaction (SSI) problems in 2D anisotropic domains. Also, an internal stress calculation scheme was established for a time domain BEM formulation used in wave propagation in anisotropic media by Liu and Zhang (2003). Finally, Denda *et al*. (2003) proposed a frequency-domain BEM for solution of eigenvalue problems involving 2D anisotropic solids with simple geometry. In more recent work (Rangelov *et al.* 2005), the Radon transformation has been used for recovering fundamental solutions, the advantage being a reduction of the governing partial differential equations to ordinary ones. The inverse Radon transformation must then be applied to the transformed solution and requires evaluation of a line integral over a unit circle, which is a much simpler task compared the integration paths previously mentioned.

1.2 Seismic wave propagation in continuously inhomogeneous media

The mathematical background behind wave motion in a continuously inhomogeneous media involves solution of partial differential equations with variable coefficients. In general, these equations do not possess explicit and easy to calculate fundamental solutions, which prevents reduction of the physical boundary-value problem (BVP) to a system of boundary integral equations that can subsequently be solved by numerical quadrature techniques. As far as work in this direction is concerned, we mention the work of Vrettos (1991) on the propagation characteristics of elastic waves (P-, S-, and Rayleigh waves) through soil deposits with vertical inhomogeneities of various types, such as the bounded exponential shear modulus and the general power law shear modulus. Manolis and Shaw 1996) derived Green functions for 2D and 3D continua using algebraic transformations that are valid for certain restricted classes of inhomogeneous materials. The present authors have produced results on wave scattering by cavities and cracks in both continuously inhomogeneous isotropic (Manolis *et al.* 2004, 2007, 2009, Dineva *et al.* 2006, 2007) and anisotropic (Dineva *et al.* 2005) solids using the BEM. These results were based on the use of closed-form fundamental solutions for restricted classes of inhomogeneous materials that were obtained by an appropriate functional transformation on the displacement vector, followed by application of the Radon transform.

1.3 Seismic wave propagation in poroelastic media

Poroelasticity accounts for the interaction between two phases, namely solid and fluid, that comprise a geological continuum. Since Biot’s (1956) pioneering contribution, the problem of wave propagation in two-phase materials has been extensively studied by many researchers. Biot (1956) assumed linear elastic material behavior for the porous solid skeleton and Darcy flow through the pores, while the interaction between deformable skeleton and fluid is described by a system of coupled partial differential equations in terms of solid displacements and fluid pressure. The BEM has seen rather limited application to dynamic poroelasticity (Kaynia and Banerjee 1992, Manolis and Beskos 1989, Kattis *et al.* 2003, Gatmiri and Jabbari 2005, Schanz and Pryl 2004, Aznarez *et al.* 2006), the reason being that fundamental solutions have a complicated mathematical form that is difficult to integrate with existing software. Also, use of Biot's equations for the synthesis of ground motions in porous geological media is still limited, due to the complexity of the underlying BVP.

In sum, the following conclusions regarding site effects in complex geological media can be drawn: (a) There is a certain paucity of work on the development of specialized BEM codes for generation of synthetic seismograms accounting for the salient mechanical properties of a geological deposit such as anisotropy, inhomogeneity and poroelasticity, the reason being difficulties in deriving appropriate fundamental solutions of the corresponding governing differential equations; (b) most of the research work to date does not concurrently take into consideration the dependence of the elastic wave signal to seismic source characteristics, wave path structure and material inhomogeneities, local geological conditions such as layering, discontinuities, surface relief, plus the presence of underground structures. This results in the absence of research results addressing a combination of different mechanical effects so as to reproduce a complex geological medium. The above observations act as motivation for the current work, where we develop and verify an efficient BEM code that intakes data produced by an independent FDM software package to generate seismic signals in a geological cross-section which contains two excavated cavities housing the underground Metro line for the Thessaloniki, Greece urban area. This particular cross section, labelled as the 'BEM box', is part of a much larger cross-section running north from the hills overlooking Thessaloniki south to the sea, which in turn is modelled by the FDM and excited by seismic wave pulses, see Fig. 2. The importance of the localized 'BEM box' stems from the fact that it accounts for complex material behaviour and geometry in the generation of free-surface ground motions that can be used as input to study the response of an important Roman monument complex situated almost directly above the Metro line tunnels.

Briefly, the paper is structured as follows. First, the BVP definition is given in Section 2. Next, Section 3 presents the hybrid FDM-BEM formulation. The handling of water-saturated soil deposits by an equivalent viscoelastic model is then discussed in Section 4, while Section 5 presents results from verification-type studies. These include the replacement of the 'BEM box' by a large finite element method (FEM) mesh so as to prove the generality of the proposed hybrid numerical scheme in Section 6, which also gives results concerning the Metro area cross-section subjected to two types of excitation: (a) a monochromatic SH-wave with frequency ω and incidence angle θ; (b) a complex SH-wave train depending on the area's seismic source characteristics, defined at bedrock and travelling upwards to the local finite region boundary. Finally, a set of conclusions summarizes our work.

2. Problem description

Consider a finite region V_1 (labeled the 'BEM box') embedded in a wider geological profile V_0, see Fig. 4. The surface of the 'BEM box' comprises the free surface S_1 plus the interface boundary Λ between V_1 and V_0. Two circular cylindrical cavities are located inside this finite region with cross-section surfaces Γ_1, Γ_2, their top at depth *d* from the free surface, and separated by center-to-center distance *e*. We introduce a Cartesian coordinate system $Ox_1x_2x_3$ and consider anti-plane wave motion, i.e., the only non-zero field variables are the displacement $u_3(\mathbf{x},\omega)$ and traction $t_3(\mathbf{x},\omega)=\sigma_{i3}(\mathbf{x},\omega)n_i(\mathbf{x})$, where $n_i(\mathbf{x}),\ i=1,2$ is the outward pointing normal vector at $\mathbf{x}=(x_1,x_2)$ and $\sigma_{i3}(\mathbf{x},\omega)$ are the shear stresses. Two BVP can now be defined:

(a) BVP 1 comprises the finite region with tunnels (i.e., the finite 'BEM box' V_1) that is a part of the larger geological cross-section of Fig. 2. Here, the dynamic load developing along boundary Λ is due to the complex seismic wave train emanating from bedrock and propagating upwards through the Thessaloniki geological deposits. This model encompasses three parts, namely the seismic source signal, the inhomogeneous wave path region and the finite-sized region. The solution technique here is hybrid comprising both FDM and BEM, with the former used to model wave propagation from bedrock to boundary Λ of the finite region. The latter method uses the aforementioned wave field on Λ as input and proceeds to solve for the seismic motions inside the 'BEM box'.

(b) BVP 2 comprises finite region V_1 with tunnels embedded in the homogeneous half-plane V_0. It is subjected to an incident, time-harmonic SH-wave polarized along the Ox_3-axis and propagating in the $x_3 = 0$ plane at an incident angle θ with respect to the Ox_1-axis. In this case, we consider complex mechanical properties for soil, namely anisotropy, inhomogeneity and poroelasticity, while the method of solution is the BEM. More specifically, we consider a monoclinic anisotropic material. This assumption is necessary, because uncoupling between plane and anti-plane strain motions for anisotropic materials is possible only if at least one elastic symmetry plane exists (Lekhnitskii 1963). Furthermore, if the Cartesian coordinate axes coincide with the principal directions of material symmetry, we then have the transversely isotropic case with two stiffness parameters c_{44}, c_{55}. If the solid is transversely isotropic, but the axis of material symmetry is along the Ox_3-axis, then conditions $c_{45} = 0$, $c_{44} = c_{55} = \mu$ hold, where μ is the soil shear modulus, while the plane $x_3 = 0$ is isotropic and characterized by two material parameters, namely μ and density ρ.

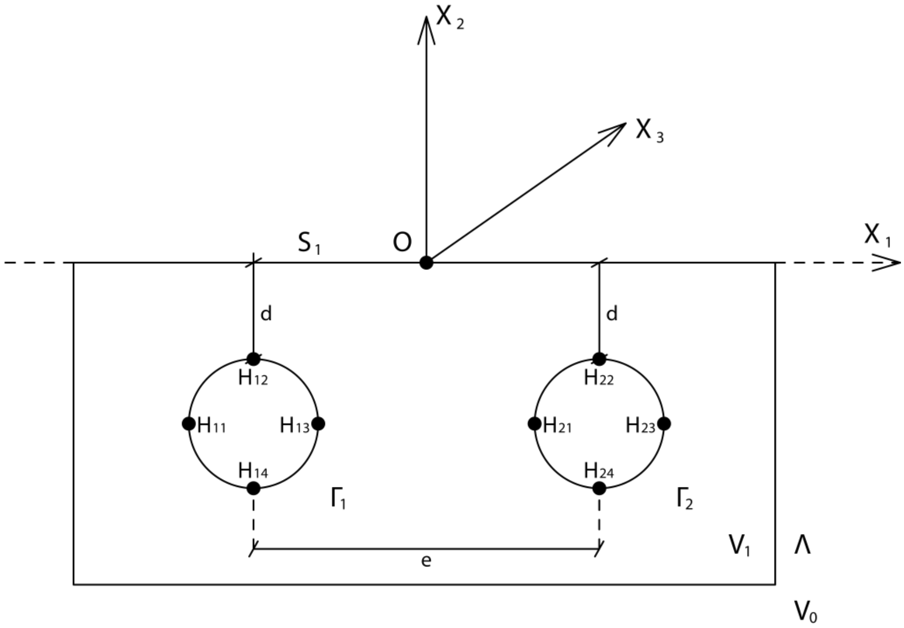

Fig. 4 Idealization (not to scale) of the finite-sized, local region V_1 ('BEM box') containing two buried Metro tunnels with surfaces Γ_1, Γ_2 and embedded in either the Thessaloniki geological deposit (BVP 1) or a homogenous half-plane V_0 (BVP 2)

2.1 BVP 1 statement

The geometry here is that of Fig. 2 and comprises the laterally inhomogeneous soil strata of region V_0 resting on bedrock where seismic waves emanate, plus the embedded, finite-sized homogeneous elastic isotropic region V_1 (the 'BEM box') with two tunnels and material properties μ^1, ρ^1. The size of the 'BEM box' is chosen so that wave backscattering into the surrounding geological strata is negligible. The objective here is to obtain synthetic seismograms at receiver points along the free surface of the local region V_1, taking into consideration: (a) the seismic source properties; (b) the laterally inhomogeneous wave path from bedrock to interface Λ; (c) the presence of the tunnels.

The governing equation describing seismic wave propagation is

$$\sigma_{i3,i} - \rho \ddot{u}_3 = 0 \quad \text{in} \quad Q_B = V_1 \ \text{x} \ (0,T) \tag{1}$$

All symbols in Eq. (1) have been previously defined, except for dots which symbolize time derivatives. The various soil layers have different material properties (see Fig. 2) and T is the duration of the seismic pulses emanating from bedrock, which for a real earthquake event would depend on the seismic source located in V_0 with known geophysical characteristics. In order to dispense with time variable *t*, the Fourier transform is applied to Eq. (1) so as to solve this BVP in the frequency domain. The resulting partial differential equation is now of the elliptic type with known fundamental solution for use in the BEM formulation applied to the 'BEM box'. Thus, BVP 1 is solved for a sufficient large frequency spectrum and the inverse fast Fourier transformation (FFT) is applied in order to recover time-dependency in the free surface seismic signal. The following boundary conditions must be satisfied, see Figs. 2 and 3: (a) zero tractions at the free surface; (b) displacement compatibility and traction equilibrium conditions at the interfaces between layers; (c) traction-free boundary conditions hold along the tunnel perimeters; (d) the seismic bed is modeled as a homogeneous half-plane with compatibility and equilibrium conditions imposed at the interface with the overburden soil deposits; (e) incoming waves are excluded from entering the inhomogeneous part of the half-plane from the seismic bed in the absence of an embedded seismic source (Sommerfeld radiation condition). Finally, solution of BVP 1 is accomplished by the hybrid FDM-BEM described below and yields the total displacement field, which satisfies a Hölder continuity condition across all boundaries defining space-time region Q_B, plus the governing equation and the boundary conditions discussed above.

2.2 BVP 2 statement

Consider the aforementioned region V_1 embedded within a homogeneous, anisotropic half-plane. We assumed a transversely isotropic material throughout, and denote the stiffness parameters and the density in V_1 as $c^1_{44}(x_2), c^1_{55}(x_2), \rho^1(x_2)$, while those of the half-plane as $\bar{c}_{44}, \bar{c}_{55}, \bar{\rho}$. Furthermore, we assume all material parameters in V_1 to vary proportionally according to the quadratic function $h(x_2) = (ax_2 + 1)^2$, i.e., $c^1_{44}(x_2) = c^0_{44}h(x_2)$, $c^1_{55}(x_2) = c^0_{55}h(x_2)$, and $\rho^1(x_2) = \rho^0 h(x_2)$, where a is the inhomogeneity parameter controlling the material gradient, while $c^0_{44}, c^0_{55}, \rho^0$ are the references values. This assumption is made because it allows recovery of fundamental solution by transform methods in closed-form (Manolis and Shaw 1996), a necessary step for the construction of BEM formulations.
The set of equations governing SH-wave motion comprise

(a) The constitutive law

$$\sigma_{13} = c_{44}^{1}\left(x_2\right)e_{13},\ \ \sigma_{23} = c_{55}^{1}\left(x_2\right)e_{23} \tag{2}$$

(b) The kinematic relations

$$e_{i3} = u_{3,i},\ \ i = 1,2 \tag{3}$$

(c) The dynamic equilibrium equation in the absence of body forces

$$\sigma_{i3,i} + \rho^{1}\left(x_2\right)\omega^2 u_3 = 0 \tag{4}$$

In the above, e_{i3} is the strain tensor, subscript commas denote partial differentiation and the summation convention over repeated indices is implied. Furthermore, we will use the notation

$$C_{ij}\left(x_2\right) = c_{44}^{1}\left(x_2\right)\ \ for\ \ i = j = 1; = 0\ \ for\ \ i \neq j; = c_{55}^{1}\left(x_2\right)\ for\ i = j = 2 \tag{5}$$

Diffraction problems in semi-infinite domains are formulated by decomposition of the total displacement and traction $\left(u_3, t_3\right)$ fields in two parts, namely the incoming free field motion $\left(u_3^f, t_3^f\right)$ plus the scattered (by the various heterogeneities) motion $\left(u_3^{sc}, t_3^{sc}\right)$. Inside region V_1, the total wave field is the sum of waves scattered by all existing boundaries, namely the tunnels surfaces, the horizontal free surface and the interface boundary Λ. Thus, the total wave field inside V_1 is $u_3 = u_3^{sc}$; $t_3 = t_3^{sc}$, while outside V_1 the total wave field is $u_3 = u_3^{sc} + u_3^f$; $t_3 = t_3^{sc} + t_3^f$. The free field motion is known and comprises incoming and reflected SH-waves from the homogeneous half-plane in the absence of defects. As incoming waves enter the finite geological region V_1, a scattered wave field is produced in the outer region as follows:

$$u_3^{sc} = u_3 - u_3^f \quad \text{and} \quad t_3^{sc} = t_3 - t_3^f \qquad \text{for} \qquad \mathbf{x} \notin V_1 \tag{6}$$

Summing up, the boundary conditions are:

(a) On the surface S_1 of the half-plane:

$$t_3\left(\mathbf{x}, \omega\right) = 0 \tag{7}$$

(b) On the tunnels surfaces Γ_1, Γ_2:

$$t_3\left(\mathbf{x}, \omega\right) = 0 \tag{8}$$

(c) On the interface boundary Λ between finite region V_1 and half-plane:

$$u_3\left(\mathbf{x} \in V_1\right) = u_3^{sc}\left(\mathbf{x} \notin V_1\right)\ \ ;\ \ t_3\left(\mathbf{x} \in V_1\right) = t_3^{sc}\left(\mathbf{x} \notin V_1\right) \tag{9}$$

with $\left(u_3^{sc}, t_3^{sc}\right)$ given by Eq. (6). Finally, the Sommerfeld radiation condition is satisfied at infinity.

The free-field wave motion $\left(u_3^f, t_3^f\right)$ of an SH-wave at any point $\mathbf{x} = \left(x_1, x_2\right)$ interior to the transversely isotropic homogeneous half-plane is computed as follows:

$$u_3^{in}\left(x_1, x_2, \omega\right) = u_0 \exp\left[-ik\left(\cos\theta\, x_1 + \sin\theta\, x_2\right)\right] + u_0 \exp\left[-ik\left(\cos\theta\, x_1 - \sin\theta\, x_2\right)\right] \tag{10}$$

$$\sigma_{i3}^{in}(\mathbf{x},\omega) = \bar{C}_{ij} u_{3,j}^{in}(\mathbf{x},\omega) \tag{11}$$

$$t_3^{in}(\mathbf{x},\omega) = \sigma_{i3}^{in}(\mathbf{x},\omega) n_i(\mathbf{x}) \tag{12}$$

In the above, the wave number and the apparent wave velocity are respectively given as $k = \omega / C_{SH}$, $C_{SH} = \left(\bar{c}_{55}\cos^2\theta + \bar{c}_{44}\sin^2\theta\right) / \bar{\rho}$, see Zhang and Gross (1998).

Summing up, the unknowns in BVP 2 are the total displacements on the free surfaces of the half-plane plus the total displacements along the tunnel perimeters Γ_1 and Γ_2. After all unknowns are determined, it is possible to reconstruct the wave field at any point inside or outside local region V_1 by use of integral representation formulae. More specifically, BVP 2 is solved by the non-hypersingular, traction-based BEM described in the next section.

3. Hybrid FDM-BEM

When modelling seismic wave propagation, the three basic components of the problem are the source, the travel path and the receiving site. In reference to this breakdown, two types of models exist in the literature:

(a) All-in-one, source–path-site unified computational tool, demanding a large amount of computer memory and time, especially when source–receiver distances are measured in the tens of km;

(b) Hybrid approaches based on a two-step procedure which combines the source and path effects computed by one method with the local site effects evaluated by another method. The wave field computed by the former method is used as input to the latter method, with the two methods appropriately connected so as to keep the formal wave-injection boundary perfectly permeable to the waves scattered by the local site.

The hybrid two-step technique originated by Alterman and Karal (1968) as a domain coupling algorithm. The same philosophy can be traced back to the work of Bielak and Christiano (1984), later expounded in Bielak *et al.* (2003). This algorithm was further extended by: (a) Fäh (1992) and co-workers (Fäh *et al.* 1990, 1993, 1994), where the modal summation and finite difference techniques were used as the first and second steps, respectively; (b) By Oprsal *et al.* (1998a, b); Oprsal and Zahradnik (2002); Galis *et al.* (2008); Zahradnik and Moczo (1996); and Moczo *et al.* (1997), who combine (in three steps) the discrete wave number method for local region computations, finite elements for the surface topography and finite differences for any localized geological structure with a flat free surface embedded in the background medium; (c) the term ‘‘wave injection’’ was introduced in Robertson and Chapman (2008) and Oprsal *et al.* (2009) as denoting efficient seismic modelling that requires various methods to be combined, with each applied to just a single task for which it is best suited. This way, the advantages of the individual methods are enhanced, while their limitations are reduced. The main disadvantage of hybrid multi-step techniques is that in subsequent steps past the first, any interaction between the backscattering waves from the local heterogeneity with the incoming wave fields emanating from the deeper layers of the geological profile is neglected. In practice, the hybrid method concept can be applied when the local heterogeneity (the tunnels in our case) are located deep inside the local region (the 'BEM box' in our case) and the backscattering from the heterogeneous part dampens out before reaching the external boundary of the 'BEM box'. This is the idea behind the 'excitation box' idea proposed by many authors who used a two-step hybrid approach. More specifically, the second step utilizes information obtained from the first step as a boundary conditions and considers wave propagation only in the 'excitation box' containing the local heterogeneities.

3.1 FDM-BEM coupling

The key point in FDM-BEM coupling is in the representation of the total wave field as the sum of free field and scattered parts, i.e., $u_3 = u_3^{sc} + u_3^f$ and $t_3 = t_3^{sc} + t_3^f$. Inside region V_1 containing the tunnel cavities, we have that total and scattered wave fields coincide, i.e. $u_3 = u_3^{sc}$ and $t_3 = t_3^{sc}$, while outside region V_1 the scattered wave field is expressed as the difference between total and free fields, i.e., $u_3^{sc} = u - u_3^f$ and $t_3^{sc} = t - t_3^f$. The boundary conditions along the interface boundary Λ couples the scattered wave fields inside and outside region V_1, satisfying the 'welded contact' condition.

In the first step of the present hybrid technique, the FDM is applied to the seismic wave propagation problem for the geological configuration shown in Fig. 2, but in the absence of the two cavities. The time-dependent FDM solution for the seismic field along the interface boundary Λ is transformed to the frequency domain and stored for use as a boundary condition in the realization of the second step. Next, BEM modelling of seismic wave propagation inside region V_1 with two cavities constitutes the second step. The size of the 'BEM box' is evaluated separately during this numerical realization so as to damped out any backscattering effects within the 'BEM box' itself.

3.2 FDM computational technique for wave motion in geological cross-sections

We use here the SH-wave FDM of Moczo (1989) for 2D problems, which was later refined by Moczo *et al.* (1996) so as to allow for a detailed representation of all irregularities in the geologic structure of a given cross-section. More specifically, this FDM permits modelling of non-flat free-surfaces if they are constrained to pass through existing grid nodes. This restriction does not apply to any other irregular interfaces present in the model. In this case, the model follows the precise irregular shapes of the subsurface topography, while appropriate material parameter values are averaged out and assigned to neighbouring nodes.

In setting up the FDM mesh, we use here a constant grid step of 2.0 m in both horizontal and vertical directions. Also, the maximum frequency for which the simulation results do not present numerical instability is 10 Hz. The grid model is bounded laterally and at the bottom with transparent, Reynolds type non-reflecting boundaries that are placed in order to avoid undesirable artificial reflections. Wave attenuation is taken into account using three relaxation mechanisms (Moczo and Bard 1993) at frequency values chosen so as to insure a constant Q in the spectrum of interest for the computations, which is from 0.1 to 10 Hz.

The seismic excitation at bedrock that gives rise to a vertically upwards propagating, planar Gabor pulse described by the following equation:

$$s(t) = \exp(-\alpha)\cos(\omega_P(t - t_S) + \psi); \quad \alpha = (\omega_P(t - t_S)/\gamma)^2 \tag{13}$$

Numerical values for the parameters appearing in the above equation are

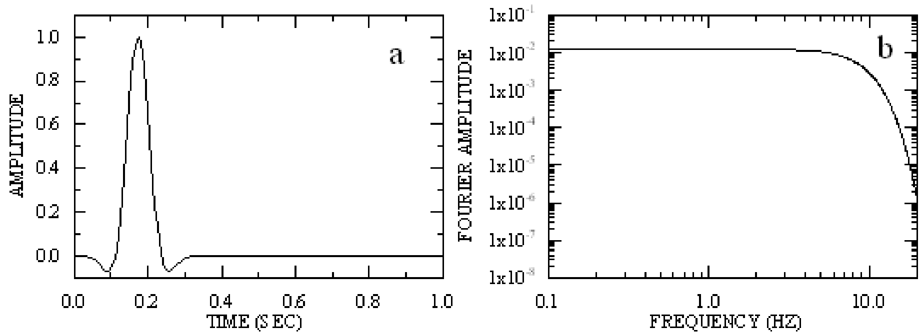

(a) (b)

Fig. 5 Gabor pulse used as seismic input at bedrock: (a) time and (b) frequency variation of the unit displacement amplitude

$f_p = 2\pi\omega_p = 0.23Hz; \gamma = 0.15; \psi = 0.0; t_S = 0.25\sec$, while Fig. 5 depicts both time variation and frequency spectrum of the normalized Gabor pulse amplitude.

3.3 BEM computational technique for wave motion inside the 'BEM box'

The BEM is now applied for solving the BVP comprising Eq. (4) plus the boundary conditions given in Eqs. (7)-(9). Note that the free-field motion (u_3^f, t_3^f) input for the seismic field along interface boundary Λ comes from the FDM solution (as the first step) under the assumption that there are no cavities.

Both the conventional displacement-based and non-hypersingular, traction-based BEM formulations are used here. Although both BEM formulations give equivalent solutions for continuous regions with smooth surface discontinuities such as cavities, the latter one is preferred over the former because it is more general in that discontinuities such as cracks can be handled (Manolis *et al.* 2012, Rangelov *et al.* 2003). After decomposition of the total wave field in free and scattered parts, the following system of boundary integral equations describes wave motion inside the region V_1:

(a) For $\mathbf{x}(x_1, x_2) \in V_1$ and $\mathbf{x}(x_1, x_2) \in \Gamma = S_1 \cup \Gamma_1 \cup \Gamma_2$, we use the non-hypersingular, traction-based BEM formulation as

$$c(\mathbf{x})t_3(\mathbf{x}) = C_{il}(x_2)n_i(\mathbf{x})\int_\Gamma [\left(\sigma^*_{\eta 3}(\mathbf{x},\mathbf{y},\omega)u_{3,\eta}(\mathbf{y}) - \rho(x_2)\omega^2 u_3^*(\mathbf{x},\mathbf{y},\omega)u_3(\mathbf{y})\right)\delta_{\lambda l}$$
$$-\sigma^*_{\lambda 3}(\mathbf{x},\mathbf{y},\omega)u_{3,l}(\mathbf{y})]n_\lambda(\mathbf{y})dS - C_{il}(x_2)n_i(\mathbf{x})\int_\Gamma u^*_{3,l}(\mathbf{x},\mathbf{y},\omega)t_3(\mathbf{y})dS, \quad \mathbf{x} \in \Gamma \tag{14}$$

(b) For $\mathbf{x}(x_1, x_2) \in \bar{\Gamma} = \Lambda$, we use the displacement-based BEM formulation as

$$c(\mathbf{x})[u_3(\mathbf{x},\omega) - u_3^f(\mathbf{x},\omega)] = \int_{\bar{\Gamma}} u_3^*(\mathbf{x},\mathbf{y},\omega)[t_3(\mathbf{x},\omega) - t_3^f(\mathbf{x},\omega)]d\bar{\Gamma} - \tag{15}$$
$$-\int_{\bar{\Gamma}} P_3^*(\mathbf{x},\mathbf{y},\omega)[u_3(\mathbf{y},\omega) - u_3^f(\mathbf{y},\omega)]d\bar{\Gamma}$$

In the above, $c(\mathbf{x})$ is the jump term that depends on the surface geometry at the collocation point; $\mathbf{x} = (x_1, x_2)$ and $\mathbf{y} = (y_1, y_2)$ are the position vectors for the observation and source points; $u_3^*(\mathbf{x},\mathbf{y},\omega)$, $\sigma_{i3}^* = C_{il}(x_2)u_{3,l}^*$ and $P_3^*(\mathbf{x},\mathbf{y},\omega) = \sigma_{i3}^*(\mathbf{x},\mathbf{y},\omega)n_i(\mathbf{y})$ are fundamental solutions of Eq. (4) for the displacement, the stresses and the traction, respectively. Both Eqs. (14) and (15) can be formulated for the inhomogeneous medium described in BVP 2, with the homogeneous case derived as default when the inhomogeneity parameter is zero, i.e. $a = 0$ and $h(x_2) = 1$.

The general fundamental solution for a quadratically-varying (with respect to depth) inhomogeneous and anisotropic material under anti-plane loading was recently derived by the authors in closed-form using the Radon transform (Manolis *et al.* 2012). Thus, $u_3^*(\mathbf{x},\xi,\omega)$ is defined as the solution at receiver point $\mathbf{x}$ for a unit point load $P(\xi)$ at the source ξ as

$$\sigma_{i3,i}^* + \rho(x_2)\omega^2 u_3^* = -P(\boldsymbol{\xi})\,\delta(\mathbf{x}-\boldsymbol{\xi}) \tag{16}$$

where δ is the Dirac delta function. The first step in the derivation is an algebraic transformation for the displacement as $u_3^* = h^{-1/2}(x_2)U_3^*$, Manolis and Shaw (1996). This way, Eq. (16) transforms into a differential equation with constant coefficients for the intermediate fundamental solution U_3^*. Secondly, after applying the Radon transform, an ordinary differential equation is obtained and solved with respect to the fundamental solution in the Radon space. The third step is to apply the inverse Radon transform and recover the fundamental solution for original displacement in the form

$$u_3^*(\mathbf{x},\boldsymbol{\xi}) = h^{-1/2}(\mathbf{x})U_3^*(\mathbf{x},\boldsymbol{\xi})\,h^{-1/2}(\boldsymbol{\xi}) \tag{17}$$

From here, the corresponding stresses and tractions can be obtained using the constitutive law. The asymptotic forms of all fundamental solutions for small arguments, i.e., when the receiver and source points coincide, are given in Manolis *et al.* (2012).

In terms of numerical implementation, we start with a discretization of all surfaces using quadratic (i.e., three node) boundary elements (BE) and apply nodal collocation to the system of boundary integral equations (14)-(15). Following evaluation of all surface integrals and imposition of the boundary conditions, an algebraic system of equations is obtained and used for solving the unknowns of the BVP in terms of the boundary data. More specifically, the shifted point scheme is applied to a given BE (this is necessary for the traction-based BEM), whereby the odd-numbered nodes and the corners are not directly used as collocation points, but are moved slightly inside the element itself to avoid singularities (Rangelov *et al.* 2003). The singular integrals converge in the Cauchy principal value (CPV) sense, because Hölder continuity requirements are fulfilled by the parabolic interpolation functions of the BE. Since the displacement fundamental solution is an integral over the unit circle, the integrals we are dealing with are two-dimensional. More specifically, two types of integrals appear, namely regular and singular, with the latter subdivided into weak (ln *r* type of singularity) and strong (1/*r* type of singularity). The regular integrals are evaluated numerically by quasi-Monte Carlo method (QMCM), while the singular ones are solved partially analytically as CPV integrals, and partially by the QMCM.

The proposed BEM methodology outlined above is suitable for the following cases involving elastic materials: (a) inhomogeneous, transversely isotropic case $c_{44} \neq c_{55}$, $a \neq 0$; (b) homogeneous, transversely isotropic case $c_{44} \neq c_{55}$, $a = 0$; (c) inhomogeneous isotropic case $c_{44}=c_{55}=\mu, a \neq 0$; (d) homogeneous isotropic case c_{44}=c_{55}= $\mu, a=0$. In BVP 2, we address cases (a)-(c), while in BVP 1, we address case (d).

4. Bardet's dynamic poroelasticity model

Consider an elastic, homogeneous and isotropic material, i.e., case (d) above. The correspondence principle of viscoelasticity (Christiensen 1971) allows for solution of viscoelastic media by a re-definition of the elastic parameters when time-harmonic conditions are assumed to hold. More specifically, for the Kelvin-Voigt viscoelastic model, the wave numbers are re-defined as $k_P^2 = \omega^2 / C_P^2(1-i\omega\xi_P)$; $k_S^2 = \omega^2 / C_S^2(1-i\omega\xi_S)$, where $C_P; C_S$ are the real parts of the P- and S-wave velocities, respectively, while $\xi_P; \xi_S$ are the corresponding attenuation coefficients representing a small amount of hysteretic damping. In the low frequency range, i.e., $\omega\xi << 1$, the wave numbers simplify as

$$k_P \approx \omega\left(1+0.5\omega\xi_P\right)/C_P\,; \quad k_S \approx \omega\left(1+0.5\omega\xi_S\right)/C_S \tag{18}$$

Bardet (1992) introduced an isomorphism by equating the wave numbers in Biot's poroelastic model with the above viscoelastic ones. By substituting the plane wave solution for the displacements in Biot's wave equation without body forces, a characteristic equation for the wave numbers can be obtained. Thus, the following equivalence relations result by equating the Biot and Kelvin-Voight wave numbers:

$$C_P = \sqrt{(P+2Q+R)/\rho_{sat}}\,; \quad C_S = \sqrt{\mu/\rho_{sat}} \tag{19}$$

$$\xi_P = \frac{\rho_{sat}}{b}\left(\frac{Q+R}{P+2Q+R} \times \frac{n\rho_f}{\rho_{sat}}\right)^2 \; ; \quad \xi_S = \frac{\rho_{sat}}{b}\left(\frac{n\rho_f}{\rho_{sat}}\right)^2 \tag{20}$$

The poroelastic material parameters appearing above are related as follows:

$$P = \frac{3(1-\nu)}{1+\nu}K_{dry} + \frac{Q^2}{R}; \quad Q = \frac{n\left(1-n-K_{dry}/K_g\right)}{1-n-K_{dry}/K_g + nK_g/K_f}K_g; \quad R = \frac{n^2 K_g}{1-n-K_{dry}/K_g + nK_g/K_f}$$

$$N = \frac{3}{2}\frac{1-2\nu}{1+\nu}K_{dry}; \quad K_{dry} = \frac{2}{3}\frac{\mu(1+\nu)}{1-2\nu}; \quad \lambda_{sat} = \lambda_{dry} + \frac{Q^2}{R} = \frac{3\nu}{1+\nu}K_{dry} + \frac{Q^2}{R} \tag{21}$$

In here, $n=V_P/V$ is the porosity of the solid skeleton, and V is a representative volume of the solid-fluid system, which comprises an elastic isotropic solid skeleton with the pore volume V_P containing a fluid. We distinguish three components of the two-phase material, namely (a) dry rock (or soil), (b) solid grain and (c) fluid. The 'dry rock' approximation is for an air-filled solid skeleton, while the 'solid grain' characteristics refer to dry rock material. The elastic bulk modulus and the density of these three components respectively are $K_{dry}, \rho_{dry} = (1-n)\rho_g$; K_g, ρ_g; K_f, ρ_f, while the solid-fluid system density is $\rho^{sat} = \rho_{dry} + n\rho_f = (1-n)\rho_g + n\rho_f$. Next, the shear strength of the porous material is provided by the solid skeleton and is not affected by the presence of the fluid, since fluids sustain dilatational deformations only. Thus, both dry and saturated soil are described by the same shear modulus, namely $\mu = \mu_{DRY} = \mu_{SAT} = 3(1-2\upsilon)/2(1+\upsilon)K_{dry}$. Furthermore, ν is Poisson's ratio for the dry skeleton, $b = n^2 g\rho_f / \hat{k}$ is the viscous dissipation coefficient, g is the acceleration of gravity and $\hat{k}$ is the soil permeability.

Morochnik and Bardet (1996) obtained the above approximate expressions for a frequency range satisfying the condition $(\omega\rho_{sat} / b) << 1$. Since permeability values for most soils is small (e.g., for sand $\hat{k} = 10^{-6} - 10^{-4}$ m/sec), this condition is easily fulfilled for the frequency range of $0.2 - 5.0$ Hz considered important in earthquake engineering. The proposed isomorphic model can also account for soil stiffening, in as much as the pore pressure induced by seismic loads helps in resisting compressive loads. This can be ascertained by inspecting Eq. (19) for the longitudinal wave velocities, while Eq. (21) shows an increase in the wave length value for λ_{SAT} as compared to that for λ_{DRY}. The isomorphic model also predicts changes in the damping mechanism for poroelastic materials. This is evident in Eqs. (19)-(21), where the phase velocities and the attenuation coefficients of the propagating waves depend on porosity, the bulk modulus of the dry skeleton, the solid grain and the fluid component, and the soil hydraulic conductivity.

Limitations of the Bardet model are: (a) it is valid in the low frequency range, (b) it cannot account for the second (slow) longitudinal wave that dampens out very fast; (c) it is impossible to account for boundary conditions involving pore fluid pressure, since we have a single phase material; (d) the consolidation process due to fluid-skeleton interaction is a time-dependent deformation process that cannot be modelled by viscoelasticity. The main advantage is mechanical simplicity, which allows for approximate solutions of BVP in fluid-saturated media by BEM.

5. Verification studies

5.1 Verification of the BEM numerical scheme

Consider first the case of a homogeneous, elastic and isotropic soil region V_1 with material constants μ^0, ρ^0 embedded in the half plane V_0 with the same material properties, as shown in Fig. 4. The incoming SH-wave moving from the far field (i.e., the half plane) into the finite region V_1 has normalized unit amplitude, vertical incidence ($\theta = \pi/2$) and propagates with non-dimensional frequency $\eta = \omega c / \pi C_{SH} = 2c / \lambda_{SH} = 0.5$. Two circular cylindrical cavities are placed in V_1 with radius *c*, depth of embedment d and center-to-center distance $e = 4c$. The coordinates of the centers of the first (left) and second (right) cavity are at $O_1(-2c,-c-d)$ and $O_2(2c,-c-d)$, respectively. We truncate the finite square region V_1 to size $b \approx 30c$ so that waves reflected across the common boundary Λ only weakly influence the cavities. For this external BVP, the BEM discretization utilizes a mesh that satisfies the following accuracy condition: $\lambda_{SH} \geq 10 l_{BE}$, where $\lambda_{SH} \geq 2\pi C_{SH} / \omega$ is the SH-wave length and l_{BE} is a typical BE length. Special attention is needed at high frequencies and for very soft soil layers, where the wavelength is small. It is clear that to reach high-numerical accuracy in these cases a very fine

BEM mesh is necessary.

It is now possible to proceed with the BEM solution in two different ways:

(a) Use of the half-plane Green's function derived by the Radon transform, which obviates free surface discretization. Thus, only discretization of the perimeters of the cavities is necessary.

(b) Use the full space fundamental solution, also derived by the Radon transform (in its general form for the inhomogeneous anisotropic cases), which however requires discretization of the free surface, of the interface boundary Λ and of the perimeters of the cavities.

Here we use both approaches and plot the surface displacement amplitude along the free surface of the half-plane in Fig. 6(a), where the separation distance is $e = 4c$, the embedment depth is $d = 5c$ and the SH-wave frequency is $\eta = 0.5$. Both solutions yield excellent accuracy when compared with the results of Lee (1977) that were obtained by a semi-analytical function expansion method for a single circular cavity in a half-plane subjected to time-harmonic SH-waves. This comparison is possible because the two cavities are placed at a large distance apart, so that their dynamic interaction is negligible. Also, modeling of an infinite half-plane is possible by truncation of the extended finite domain. Next, Fig. 6(b) compares both BEM solutions for surface displacement amplitudes at $\eta = 0.4$ versus x_1 / c for the same scenario described previously, but now the cavities are at depth $d = 2c$ and have a separation distance $e = 0.5c$. At this proximity, the dynamic cavity interaction effect is pronounced and must be taken into consideration. Excellent agreement is observed here between the results obtained by the two different BEM computational schemes, namely one using the Green's function for half-plane and another using the fundamental solution for the full plane with a truncated surface mesh.

5.2 Verification of Bardet's model for pressure wave propagation

The second series of numerical examples utilizes Bardet's viscoelastic isomorphism model to study wave motion in a poroelastic deposit embedded in the poroelastic half-plane. Both deposit and the surrounding half-plane have the same material properties. We have to considered P-wave propagation in this water-saturated continuum. Thus, the following two solutions are compared: (a) the first is obtained by Lin *et al.* (2001, 2005), where Biot's model is used and results are presented for drained boundary conditions and for an inviscid pore fluid; (b) the second is obtained by the BEM for the aforementioned deposit embedded in the half-plane, with mechanical properties based on the Bardet model. The material examined is sandstone (Lin *et al.* 2001, 2005): with $K_q = 36000$ MPa; $\rho_q = 2650$ kg/m^3; $\rho_f = 1000$ kg/m^3; $K_f = 2000$ MPa. Also, the porosity, Poisson' ratio and the solid stiffness ratio variation respectively are $n = 0.3$; $\nu = 0.25$; $\mu^{\mathbf{0}} / K_f = 0.1, 1.0, 10.0$. Fig. 7 plots these solutions for the horizontal and vertical surface displacement amplitudes versus incident angle of the time-harmonic P-wave. The plots show that both models yield very similar, nearly identical, results. This implies that the simpler, equivalent viscoelastic model can be used successfully to approximate poroelastic effects. Fig. 7 also shows the amplitude of the horizontal displacement decreasing with increasing solid stiffness, with the purely elastic medium response serving as an upper bound. The vertical displacement, however is practically unaffected by the presence of poroelasticity for the P-wave excitation.

5.3 Verification of the hybrid FDM-BEM scheme

Verification of the hybrid FDM-BEM scheme is done by solution of BVP 1 defined for the geological cross-section shown in Fig. 2, but without the presence of tunnels. This problem is solved in frequency domain in the following two ways: (a) a pure FDM, which yields the

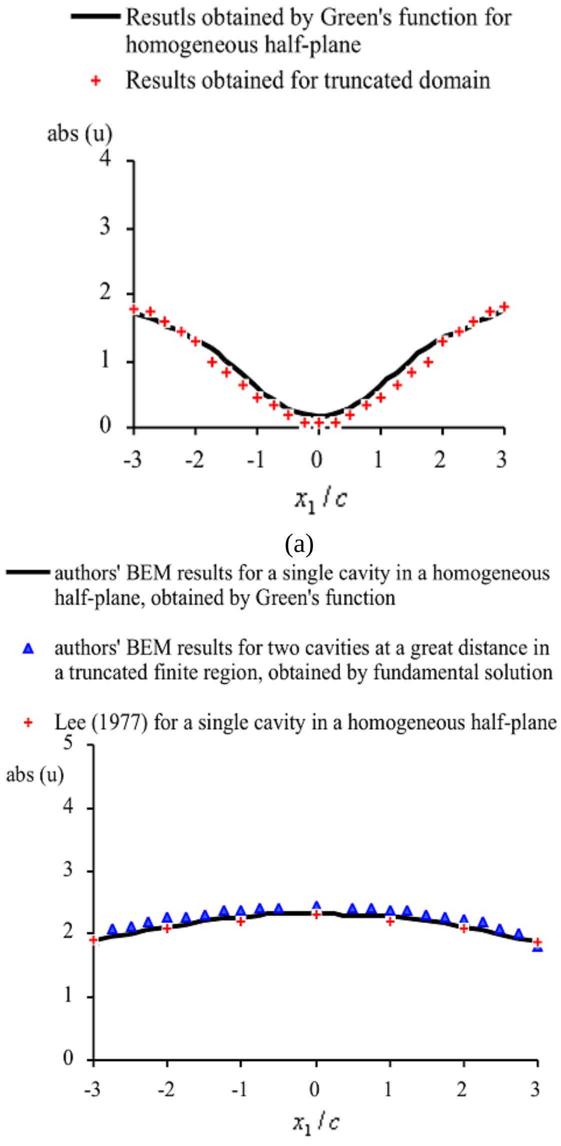

Fig. 6 Surface displacement amplitude for a half-plane with two embedded circular cavities of radius c swept by an SH-wave with incident angle $\theta = \pi / 2$: (a) separation distance $e = 4c$, embedment depth $d = 5c$ and frequency $\eta = 0.5$; (b) separation distance $e = 0.5c$, embedment depth $d = 2c$ and frequency $\eta = 0.4$

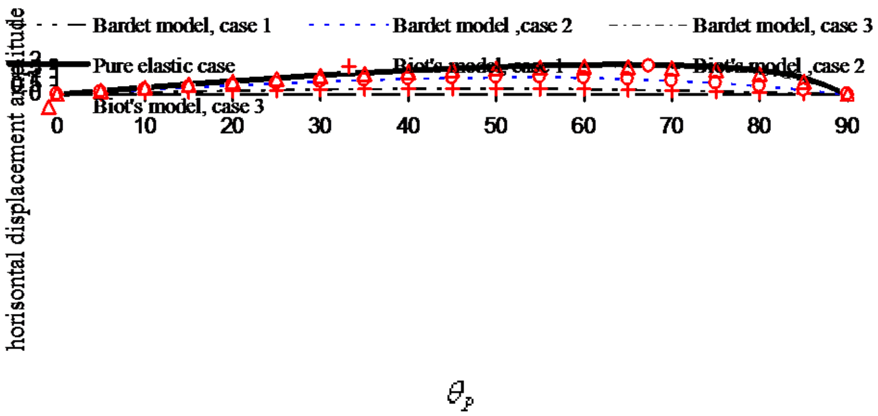

(a)

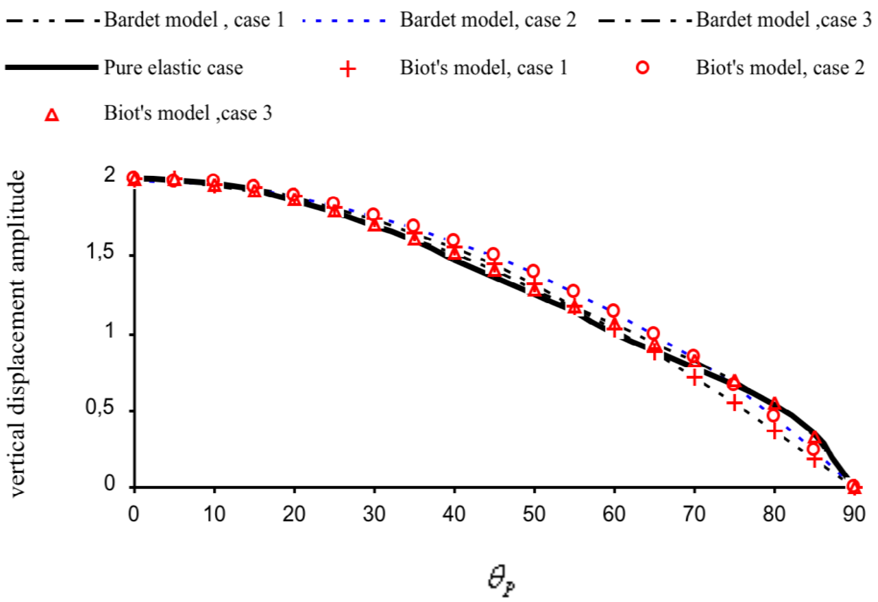

(b)

Fig. 7 Displacement amplitudes (a) u_1 and (b) u_2 at the free surface of a homogeneous poroelastic half-space versus a P-wave incident wave angle θ_p: Comparison of the Biot (1956) and Bardet (1992) models with Cases 1, 2, 3 corresponding to $\mu^0 / K_f = 0.1, 1.0, 10.0$

displacement solution across the free surface of region V_1 (note the FDM solution is in time domain and an FFT is needed to recast results in the frequency domain) ; (b) the two-step hybrid technique, with (i) application of the FDM for computation (and storage) of the wave field along the interface boundary Λ; and (ii) recovery of this wave field and subsequent input as a BEM boundary condition to solve for the BVP comprising wave motion inside and outside region V_1, but within the 'BEM box' bounds. Following the second step, displacements along the free surface of region V_1 are obtained and compared with the pure FDM results.

Detailed data on the mechanical properties of the geological cross-section are given in Raptakis *et al.* (2004a) and some basic information is shown in Fig. 2. The excitation is a vertically incident SH-wave with the displacement time variation given in Eq. (13), namely a Gabor pulse. Figs. 8 and 9 compare the results obtained by both approaches that were outlined above, at two control points CL(870,26); CR(950, 28) (in m) along free surface S_1, near the left and right edges of the Metro station area cross-section in Fig. 3. We observe very good agreement between both sets of results, which demonstrates the high accuracy achieved by the proposed hybrid approach. In general, comparison studies between the pure FDM and hybrid techniques help establish accuracy bounds on the latter ones, given the possibility to define discretized areas common to both approaches. A similar type of verification study can be found in Fäh (1992), where a hybrid modal summation-finite difference method (MS-FDM) was verified against a background 1D model that was also solved by the analytical modal summation method (MSM). Another benchmark example was done by the Wuttke *et al.* (2011), which helped verify a hybrid computational tool comprising the wave number integration method (WNIM) and the BEM. In this particular example, the material inside 'BEM box' was assumed homogeneous, although it is not restriction since the type of BEM formulation desired is based on the type of fundamental solutions available.

6. Case study for a Thessaloniki metro station

In what follows, we present the results of a parametric study, which aims to reveal the complex character of the seismic wave fields that develop in real geological profiles. More specifically, we focus on a cross-section of the city centre of Thessaloniki, Greece, see Figs. 1 and 2. Within this large cross-section spanning 1.5 km from the foothills of Mount Hortiaitis to the north to the Gulf of Thermaikos to the south, we discern a smaller, fictitious box-like inclusion (the 'BEM box'). This inclusion contains the two parallel-running tunnels of the Thessaloniki Metro line, while the important historical Roman monument complex known as the Rotunda with the Arch of Galerius are located at the surface, almost directly above the tunnels. This finite geological region is for studying site effects, while its geometry is depicted in Figs. 3 and 4. Concurrently, we present numerical simulations when the two tunnels are located in a half-plane and subjected to time-harmonic SH-waves. In this last case, the surrounding half-plane is anisotropic, continuously inhomogeneous and/or poroelastic and assigned the same material properties as the finite-sized region.

6.1 Two tunnels in the homogenous isotropic half-plane under SH-waves

We start with the finite region V_1 modeled as a homogeneous, elastic and isotropic continuum with density $\rho^0 = 1{,}885$ kg/m^3 and shear modulus $\mu^0 = 296{,}800$ kN/m^2. In turn, the region is embedded in a homogeneous, isotropic half-plane with the same material properties. The region itself is a nearly rectangular box with dimensions 100×48 m (note the free surface has a gentle

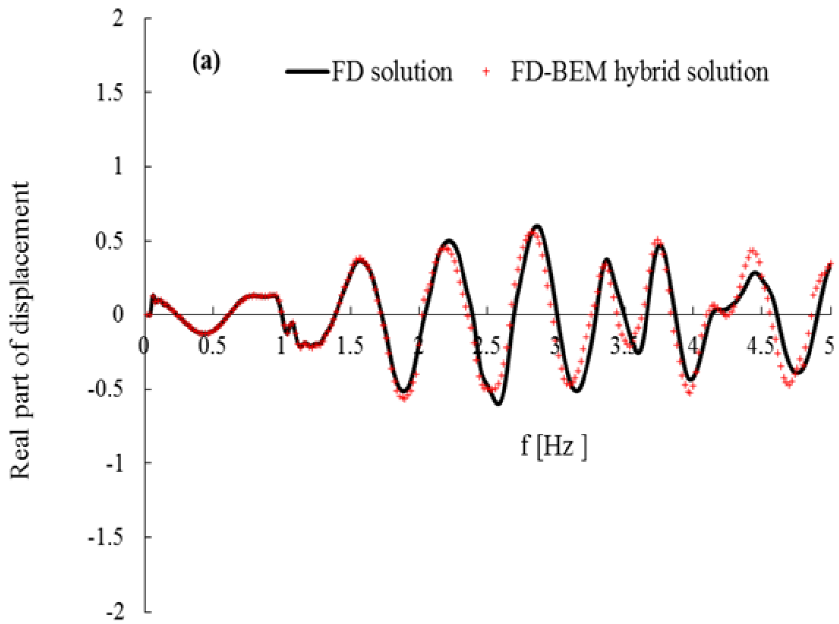

(a)

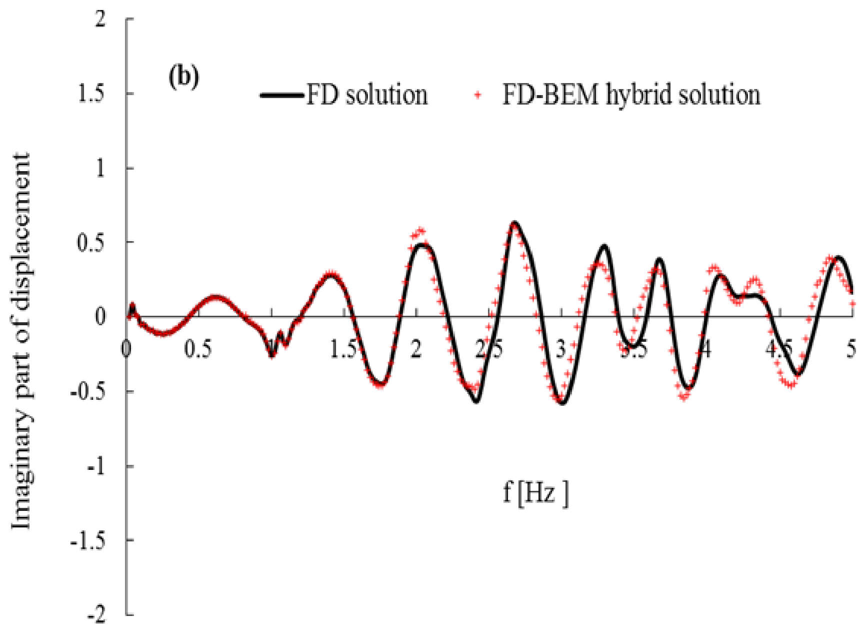

(b)

Fig. 8 Displacement versus frequency at the left control point CL: (a) Real part and (b) imaginary part of the displacement as obtained by the FDM and the hybrid FDM-BEM

slope of about 1% from north to south). Next, we define the non-dimensional frequency of vibration as $\Omega = \omega c / C_{SH} = 2\pi c / \lambda_{SH}$, where $C_{SH} = 400\, m/s$ is the wave speed and λ_{SH} is the corresponding wavelength of the incident SH-wave, while c is a representative cavity dimension (e.g., the radius for a circular one). We introduce a coordinate system Ox_1x_2 centered at $O(910, 24)$, see Figs. 3 and 4, and proceed to discretize all boundaries of the region. More specifically, we only use six BE per vertical outer boundary, while ten BE are used along each horizontal outer boundary and twelve BE are used per cavity perimeter. Note that the separation distance between the cavities is e = 6 m and that they are both placed at a depth d = 22 m from the free surface. The left cavity is situated at a distance of 40 m away from the left vertical

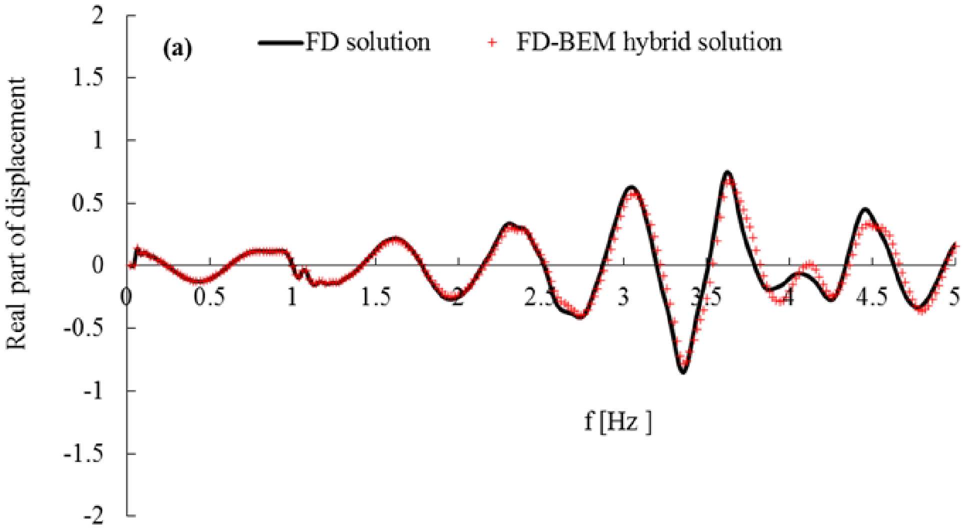

(a)

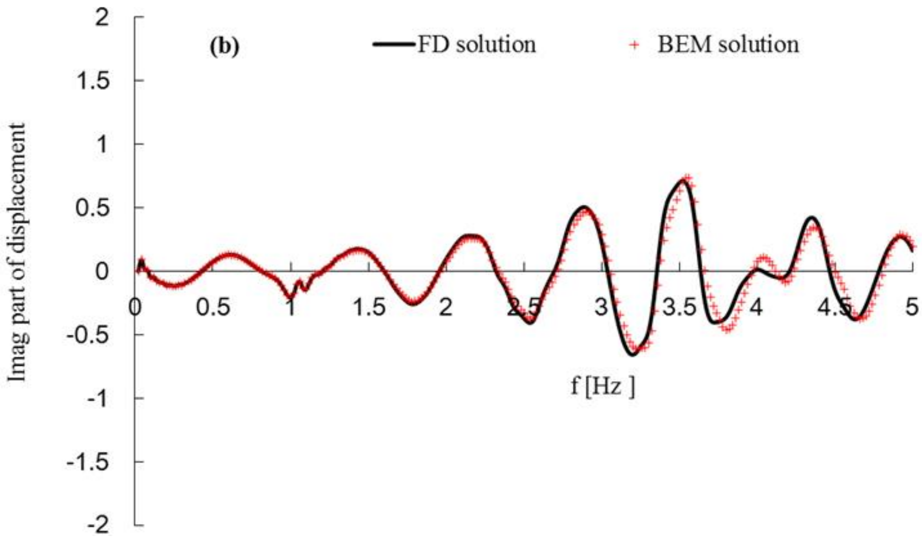

(b)

Fig. 9 Displacement versus frequency at the right control point CR: (a) Real part and (b) imaginary part of the displacement as obtained by the FDM and the hybrid FDM-BEM boundary, while the right cavity is 42 m from the right one. Finally, we define two control (or observation) points on the free surface, namely the midpoint *A*(910, 26) between the two cavities and the Rotunda monument position *R*(940, 28).

The first series of results are plotted in Fig. 10 as the displacement amplitude distribution along the free surface of the finite region V_1 at three values of non-dimensional frequency $\Omega = 0.1; 0.3; 0.5$ and for vertical SH-wave incidence. We observe that the displacement distribution becomes more oscillatory with increasing wave frequency, although the maximum magnitude values do not change appreciably. What is interesting at higher frequencies where the signal wavelength becomes comparable to the cavity dimension (say at about 10:1), is the appearance of displacement 'troughs' at precisely the cavity epicentres (i.e., the surface projection of the cavity centres). This seems to suggest an indirect way for locating the cavities from surface measurements. Next, the effect of incident SH-wave direction, namely $\theta = 90^0; 60^0; 30^0$ is shown in Fig. 11, where the displacement amplitude is plotted versus non-dimensional frequency Ω at the two aforementioned control points *A, R*. Again the same picture emerges, which is quite clear for vertical wave incidence and less so for other angles of attack, namely the appearance of 'spikes' at the control points for certain frequency bands, which progressively become larger in magnitude as the frequency increases.

The second series of results in Figs. 12 and 13 plot the normalized displacement amplitude as a function of frequency Ω at observation points along the perimeter of both circular cavities. More specifically, these points are: (a) Left cavity mid-points $H11(900,3); H12(903,6); H13(906,3)$ on the left vertical, upper horizontal and right vertical perimeters, respectively (see Fig. 3 coordinate system); (b) right cavity mid-points $H21(912,3); H22(915,6)$ on the left vertical and upper horizontal perimeters, respectively. Figs. 12 and 13 are for the left and right cavity observation points, respectively, and for two SH-wave incidence angles of $\theta = \pi/2; \theta = \pi/6$. From these figures we deduce that the presence of two cavities produces noticeable interaction effects with the free surface, as manifested by the fact that we observe a six-fold increase for the two observation points on the upper side of the cavities (as compared to the lower sides), irrespective of SH-wave incidence angle. These values are to be contrasted with the cavity-to-cavity interaction phenomenon, where for observation points along the perimeter facing each other, we observe maximum amplification values of about four. In all cases, the maximum amplification values occur at the higher frequency range, where the incident SH-wave length becomes comparable to the cavity dimensions and to the depth of embedment.

6.2 Two tunnels in the poroelastic half-plane under SH-waves

The next series of numerical simulations focus on a water saturated soil finite region, where the dynamic response is recovered through use of the Bardet (1992) viscoelastic isomorphism. Following Lin et al. (2101), the soil's dry bulk modulus depends linearly on porosity as

$$K_{dry} = K_{cr} + (1 - n/n_{cr})(K_g - K_{cr}) \tag{22}$$

where $K_{cr} = 2{,}000$ MPa is the bulk modulus at critical porosity $n_{cr} = 0.36$. The values for poroelastic soil are approximated as follows:

$$K_g = 36{,}000 MPa;\ \rho_g = 2{,}650\, kg/m^3;\ \rho_f = 1{,}000\, kg/m^3; K_f = 2000 MPa;\ \hat{k} = 10^{-6} \tag{23}$$

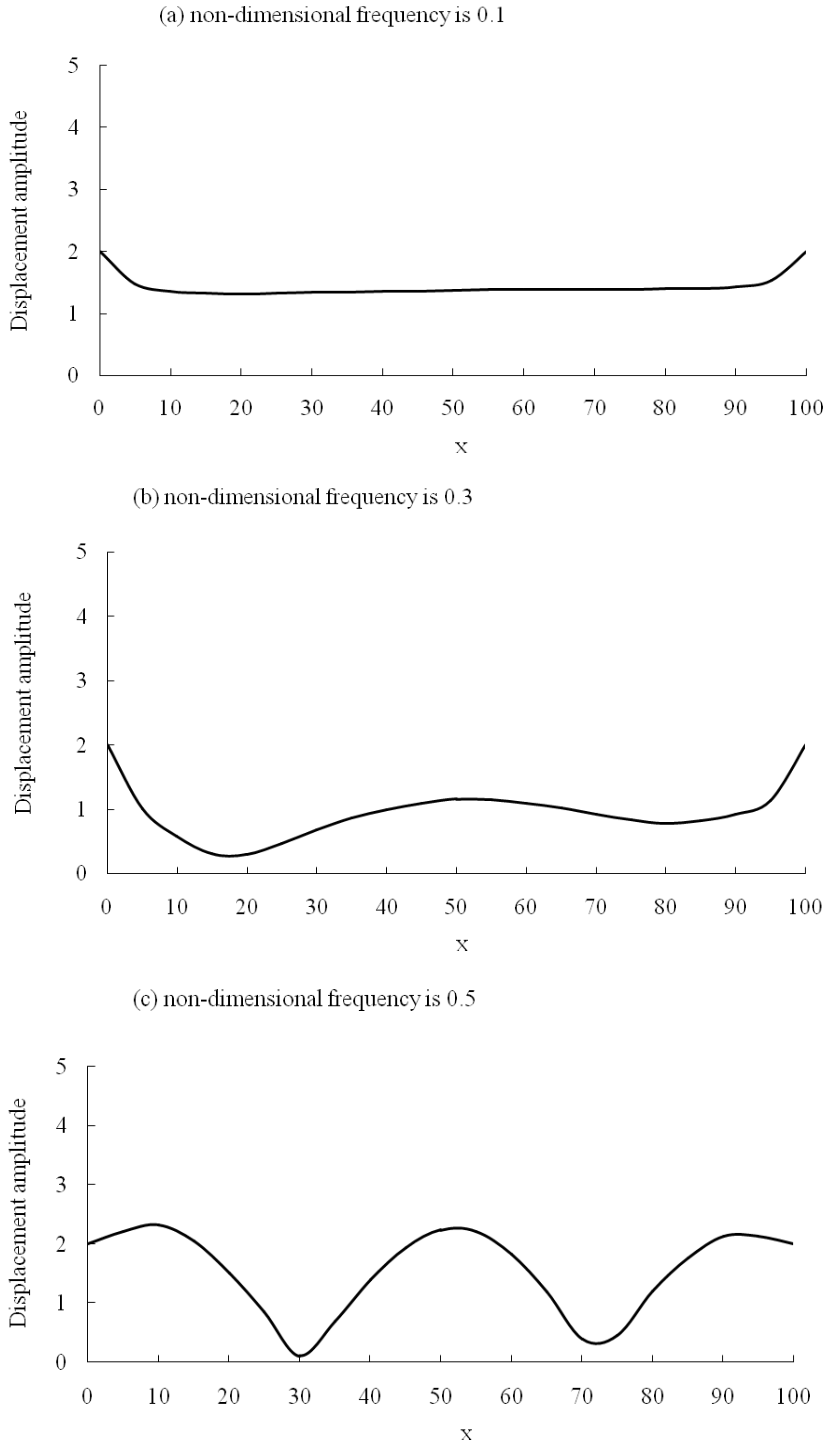

Fig.10 Displacement amplitude distribution for vertical SH-wave incidence along the free surface of the homogeneous isotropic half-plane with tunnels: (a) $\Omega = 0.1$, (b) $\Omega = 0.3$ and (c) $\Omega = 0.5$

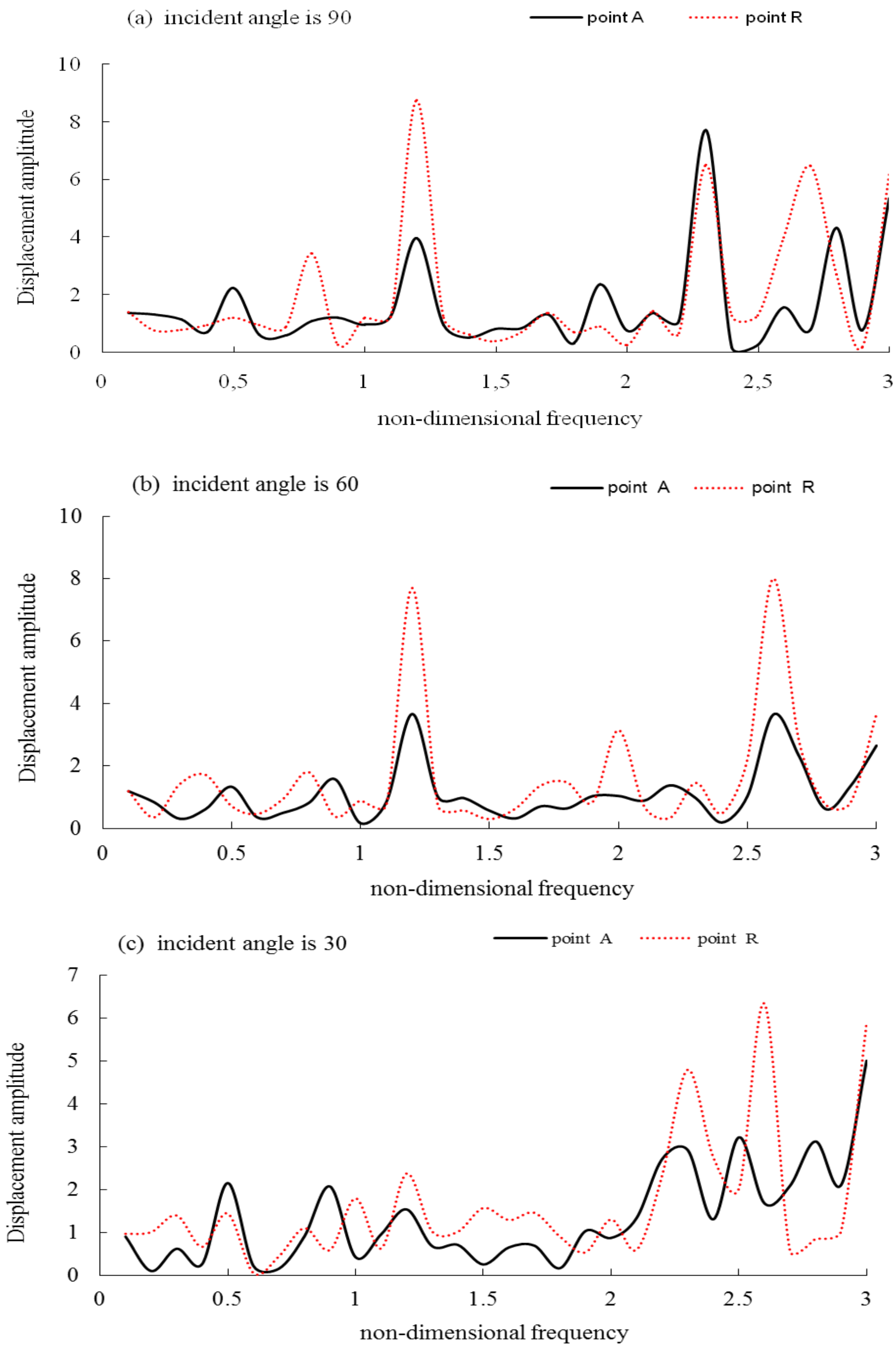

Fig. 11 Displacement amplitude vs. frequency at control points A, R on the free surface of a homogeneous isotropic half-plane with tunnels for SH-wave incidence angles: (a) $\theta = 90^0$, (b) $\theta = 60^0$ and (c) $\theta = 30^0$

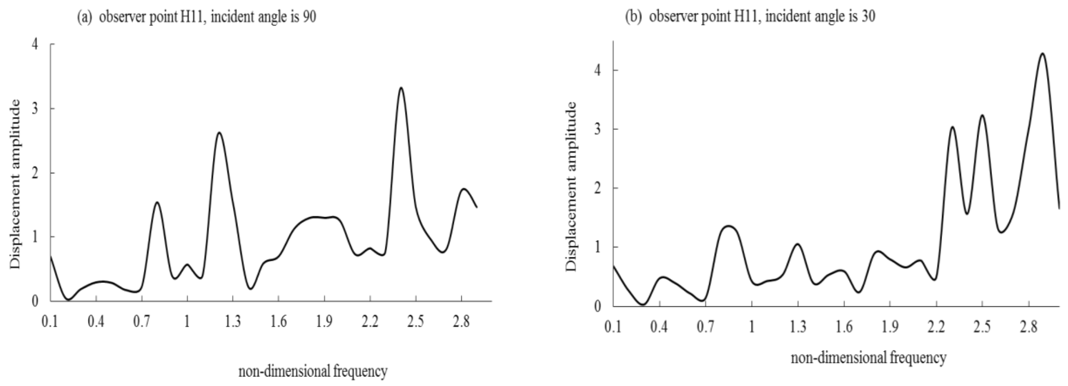

(a)

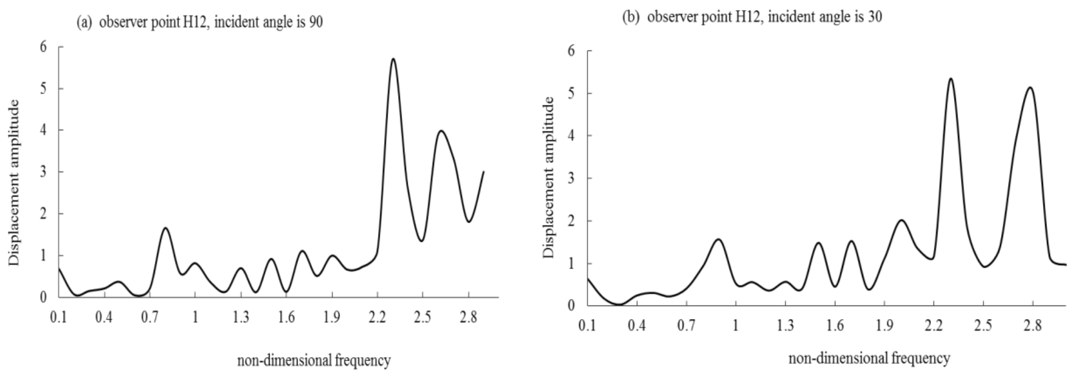

(b)

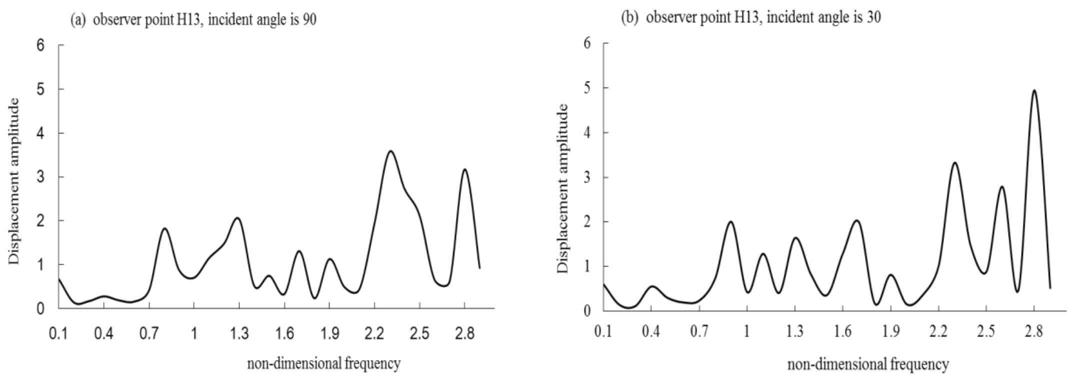

(c)

Fig. 12 Displacement amplitude vs. frequency Ω along the left cavity perimeter in the homogeneous isotropic half-plane at observation points (a) *H*11, (b) *H*12, (c) *H*13 and for two values of wave incidence

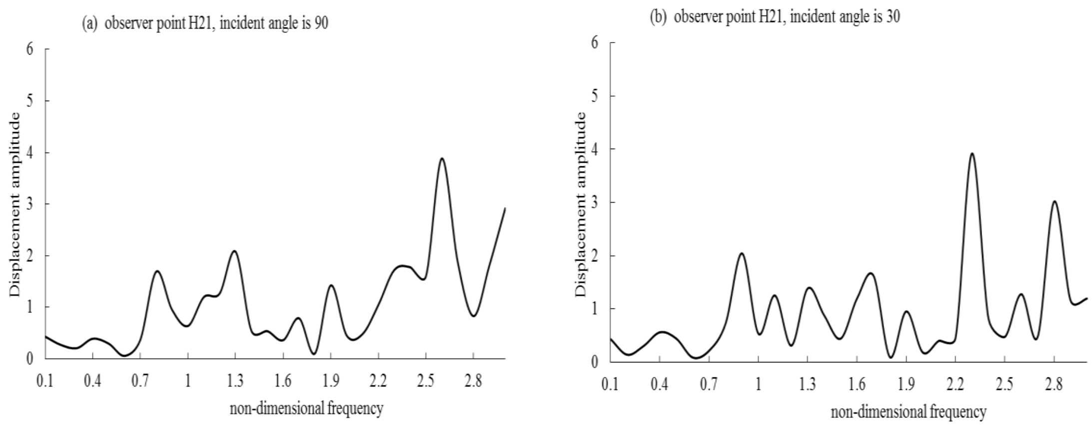

(a)

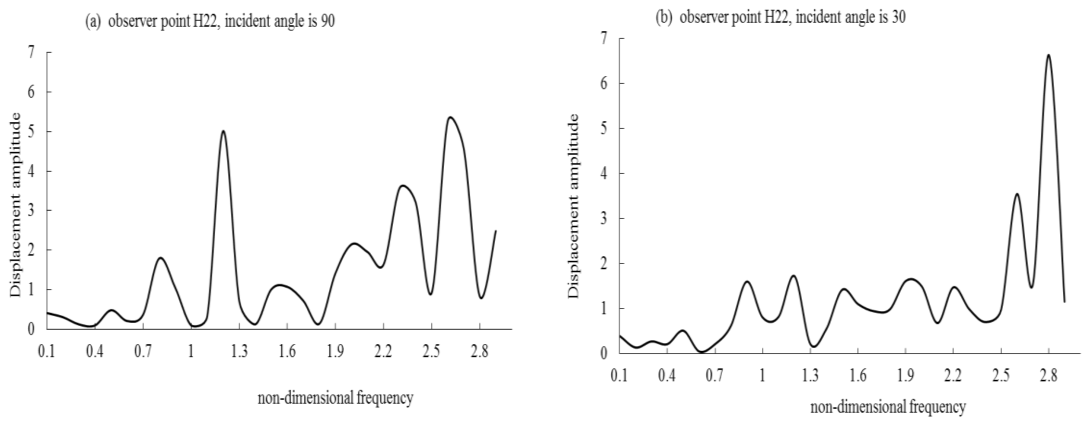

(b)

Fig. 13 Displacement amplitude vs. frequency Ω along the right cavity perimeter in the homogeneous isotropic half-plane at observation points (a) *H*21; (b) *H*22 and for two values of SH-wave incidence

Fig. 14 compares results for the displacement amplitude along the free surface of the poroelastic inclusion at three different non-dimensional frequency values of $\Omega = 0.1; 0.3; 1.5$ for the normally incident SH-wave. Two porosity values are considered, namely *n* = 0.1; *n* = 0.35. We note that the former value corresponds to a poroelastic material whose dynamic response is nearly identical to that an elastic solid, a fact that has been confirmed in past work by Knopoff *et al.* (1957). As was the case with the verification study in Section 5, water saturation in the soil is responsible for the emergence of damping effects that result in a less pronounced, smoother displacement response as compared to dry soil. Porosity does not seem to play much of a role in water saturated soils, at least in the lower frequency range. The same is not true for dry soil, where high porosity values at higher frequencies result in a more pronounced displacement response, typical of a lighter, less stiff deposit. Next, in Fig. 15 we switch to plots involving fixed observation points A and R and allow the frequency Ω to vary. Again we observe the equivalent damping effect due to the presence of water. More specifically, in the dry case and for a high porosity value, we observe a sharp peak in the displacement amplitude at around $\Omega = 2$, where the ratio of cavity side length to SH-wave length is $c/\lambda_{SH} = 1/\pi$. In sum, poroelasticty as represented by Bardet's model shows a stiffening effect for water saturated soils since Lame's constant $\lambda_{SAT} > \lambda_{DRY}$ and a damping effect is present that is frequency dependent. This last effect depends on the ratio $K_g > K_f$. If $K_g >> K_f$, poroelasticity effects are negligible, but become noticeable as the stiffness of the dry skeleton decreases.

6.3 Two tunnels in the homogeneous anisotropic half-plane under SH-waves

The influence of the soil anisotropy is demonstrated in Fig. 16, where the displacement amplitude across the free surface is plotted at three dimensionless frequency values of $\Omega = 0.1; 0.5; 1.5$. More specifically, the geological finite-sized inclusion remains homogeneous, but we introduce orthotropic material behaviour and utilize the following values for the soil material properties:

$$C_{44} = 0.2968 \times 10^9 Pa; \quad C_{55} = m C_{44}; \quad m = 1.0; 0.55; 1.5; 2.5; \quad \rho = 1{,}855 kg/m^3 \qquad (24)$$

At low frequencies, we observe the effect of anisotropy on the displacements to be negligible, but as frequency increases the surface displacement frequency 'snapshot' becomes incoherent and diverges from the isotropic case m = 1. Obviously, the presence of different amounts of stiffness along the two principal directions produces dispersion phenomena that destroy the orderly and predictable wave motion hitherto observed in the isotropic and homogeneous material case.

6.4 Two tunnels in the inhomogeneous isotropic half-plane under SH-waves

In this final preliminary series of numerical results, the inhomogeneous, isotropic half-plane containing the embedded finite-size region with the two tunnels is swept by an incoming SH-wave. We first plot the shear modulus variability with depth in Fig. 17. The controlling parameter for this continuously inhomogeneous deposit is coefficient a in the dimensionless material function $h(x_2) = (ax_2 + 1)^2$, which was introduced in Section 2 and corresponds to a quadratic variation of the shear modulus and of the density with respect to depth. Values for coefficient a are assigned by interpolation of soil strata stiffness from the geological profile in Fig. 2 and are listed in Table 1. Next, Fig. 18 investigates this material gradient effect on the displacement distribution along the free surface of the geological profile for three dimensionless frequency Ω values. The plots are parametric in terms of values for a = $0; -0.002; -0.008; -0.0138$. A comparison of all these results shows that material inhomogeneity is manifested in equal measure at all three frequencies examined, i.e., the response increases proportional by roughly $5\%; \ 15\%; \ 25\%$ when compared to the homogenous material case of a = 0. These values correspond to a smooth drop in the shear modulus value from bottom to top of $80\%; \ 30\%; \ 5\%$, respectively, indicating a soil deposit that becomes weaker as it approaches the free surface. A consequence of this particular mechanical model is that the soil density suffers a similar drop, so macroscopically the shear wave velocity appears constant.

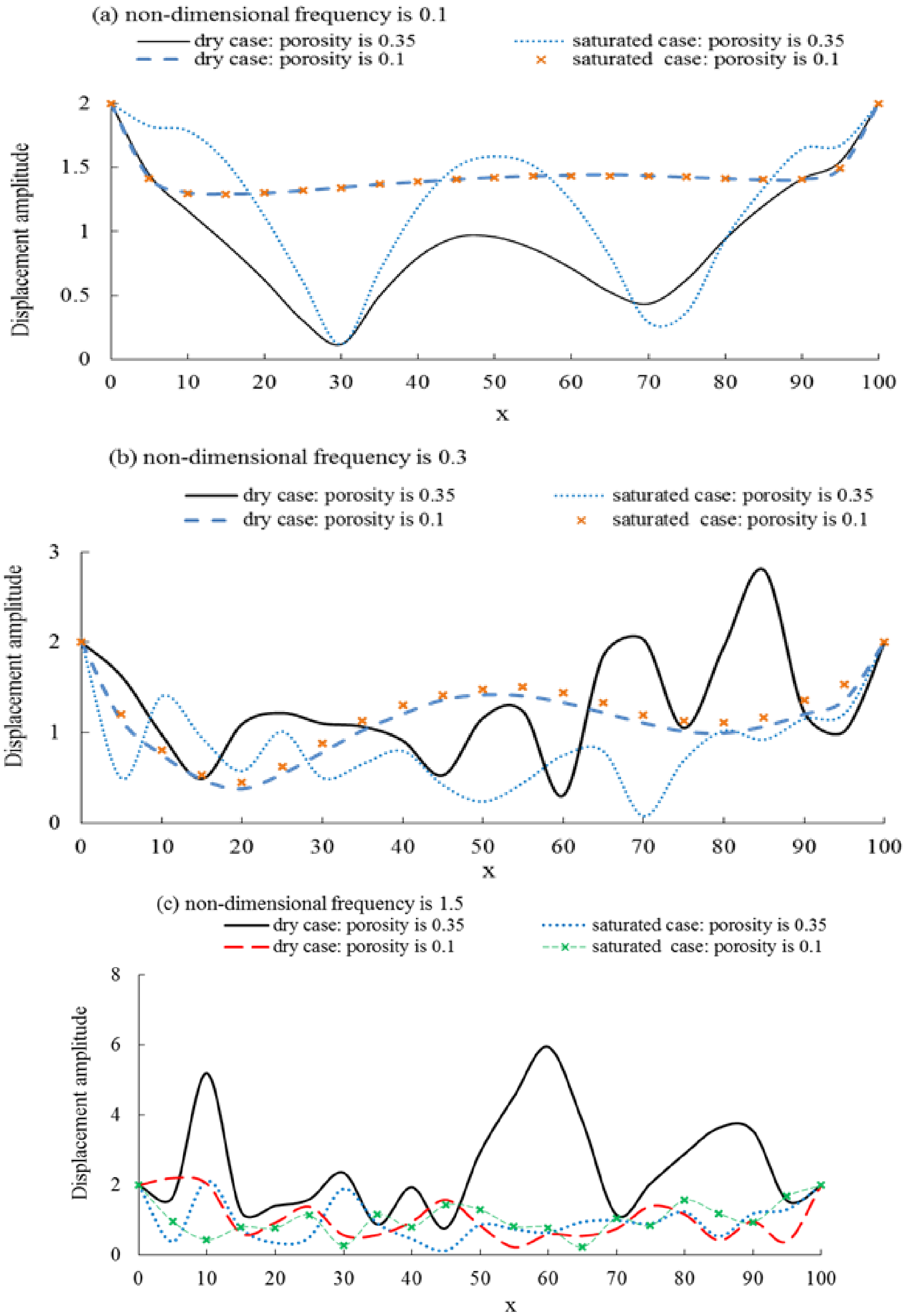

Fig. 14 Displacement amplitude along the traction-free horizontal surface of the poroelastic half-plane enclosing a finite geological region with tunnels for both dry and saturated soil cases and at three non-dimensional frequencies: (a) $\Omega = 0.1$; (b) $\Omega = 0.3$ and (c) $\Omega = 1.5$

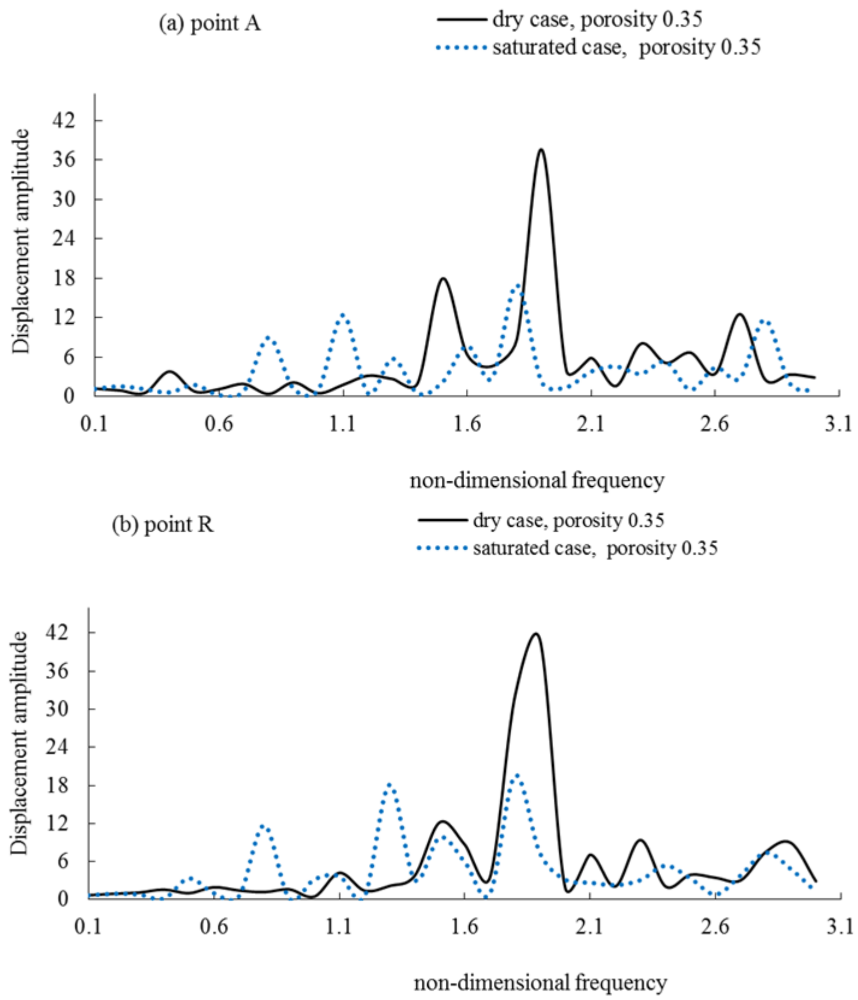

Fig. 15 Displacement amplitude versus frequency Ω at two observation points at the free surface of the poroelastic half-plane enclosing a finite geological region with tunnels: (a) point A and (b) point R

6.5 Response of the Metro tunnels embedded in the 'BEM box' to a Gabor pulse

In this set of results, we compute the frequency-dependent displacement amplitudes at observation points *H11(900,3), H12(903,6), H13(906,3*), *H14(903,0)* (in m) clockwise along the perimeter of the left cavity, and at observer points *H21(912,3), H22(915,6), H23(918,3), H24(915,0)*, also clockwise along the perimeter of the right cavity, as marked in Figs. 3 and 4. These two sets of frequency plots are shown in Figs. 19 and 20, respectively. Normalization is by dividing with the maximum amplitude recorded at the 'epicenter' points along the free surface corresponding to these observer points, and in the absence of tunnels. The seismic source is the Gabor pulse given in Eq. (13), which is applied across the base of the Thessaloniki cross-section of Fig. 2. In essence, this is BVP 1 solved using the hybrid FDM-BEM as described in Section 3.

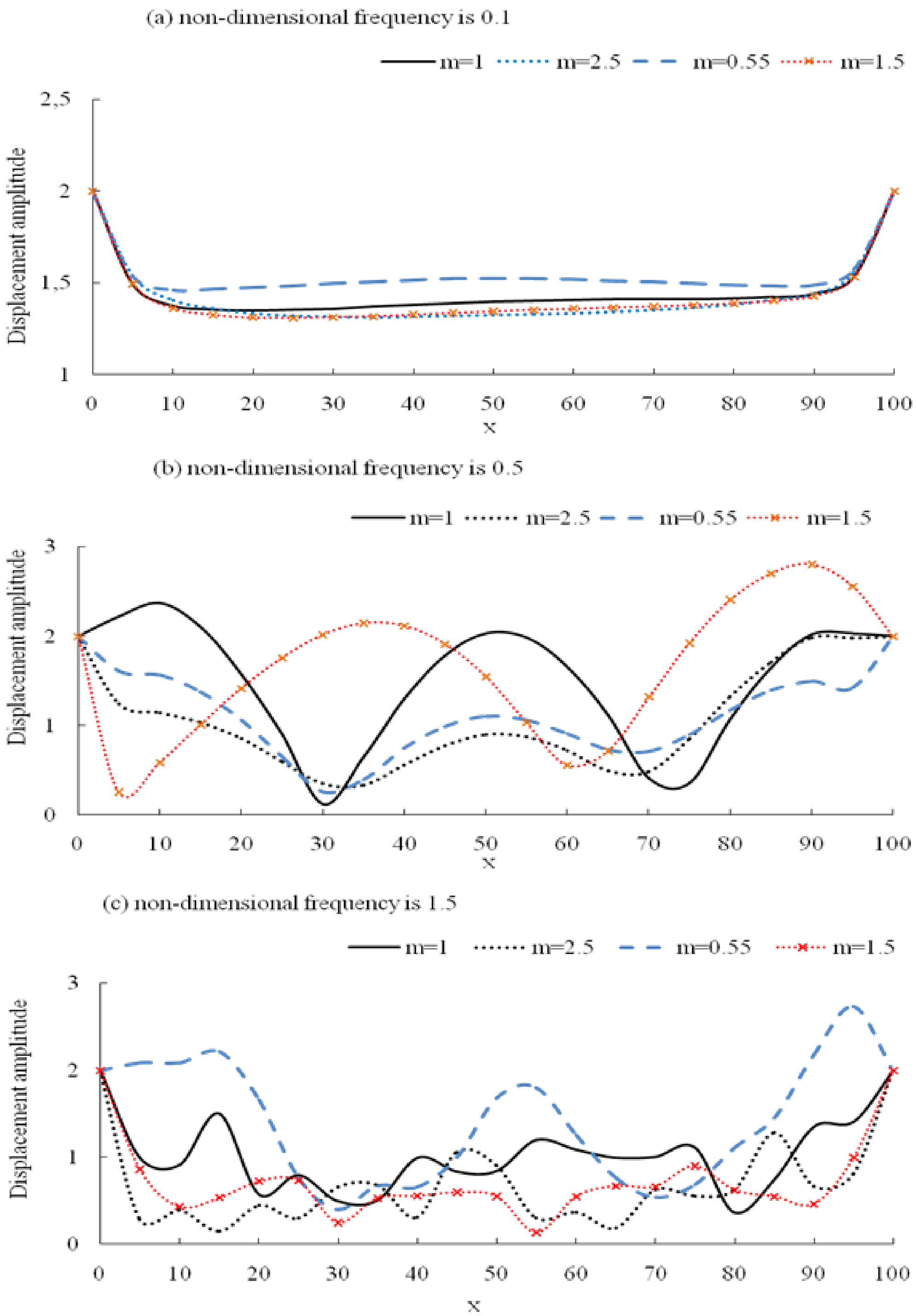

Fig. 16 Displacement amplitude along the free surface of a homogeneous orthotropic half-plane enclosing a finite geological region with tunnels at different values of parameter $m = c_{55} / c_{44}$ and for three dimensionless frequency values: (a) $\Omega = 0.1$; (b) $\Omega = 0.5$; (c) $\Omega = 1.5$

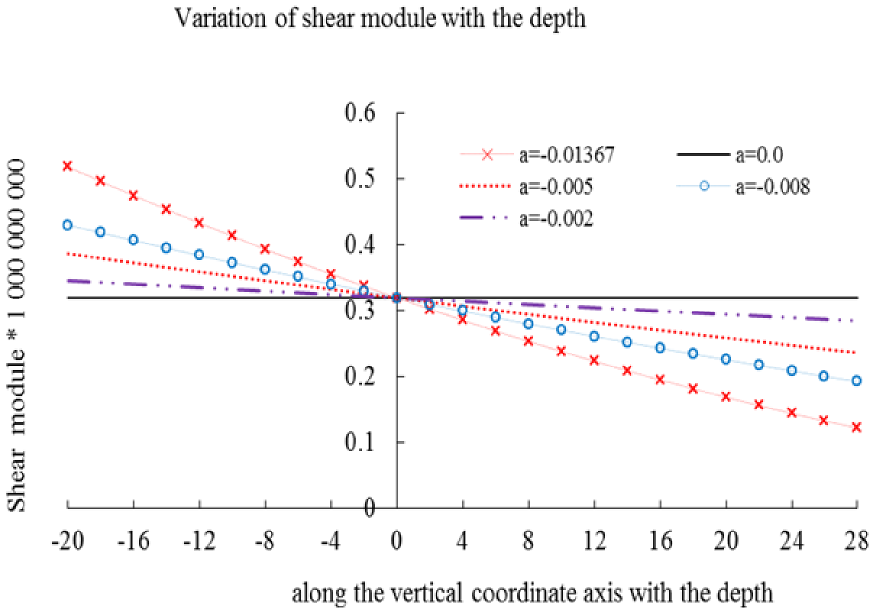

Fig. 17 Soil shear modulus $\mu = \mu(x_2)$ variation with depth in the continously inhomogeneous, isotropic finite region embedded in the surrounding half-plane

Table 1 Material properties of the local geological profile around the Metro tunnels

Layer	Cover depth d (m)	Material density ρ (kg/m^3)	SH-wave speed C_{SH} (m/s)	Stiffness coefficient C_{44} (kN/m^2)	Stiffness coefficient C_{55} (kN/m^2)
1	30	1850	250	115,625	173,438
2	0	2000	400	320,000	480,000
3	-20	2100	600	756,000	1,134,000

Given that the Gabor pulse is practically a white noise signal (i.e., all frequencies have the same excitation amplitude) in the smaller than $10\,Hz$ frequency range, the soil response is basically a transfer function that clearly shows the first two resonant frequencies in the 'BEM box' with the tunnels, which are about $2.0\,Hz$ and $4.8\,Hz$. This is true in nearly all sub-plots, where it should be noticed that the input to the 'BEM box' comes from surrounding soil strata that are not horizontal, and neither is the 'BEM box' centered. Thus, the left cavity receives a more pronounced input and the corresponding sub-plots show the resonant frequencies more clearly than those of the right cavity.

Next, Fig. 21 demonstrates the influence of the tunnels on the signals that develops along the free surface, and in particular at the site where the Rotunda monument complex is located, see Fig. 3. The frequency spectra at the relevant observation point R clearly show the response peaks caused by the buried tunnels, especially at the resonant frequencies. This is in contrast to the case where cavities are absent, which yields a displacement spectrum is rather flat with low amplitude. The corresponding time histories at R are produced by inverse FFT of the frequency spectra, using an envelope function (i.e., a taper) to suppress any spurious motion at the beginning

$(t \leq 1.0\,\text{sec})$and the end $(t \geq 14.0\,\text{sec})$ of the time spectrum. These are all plotted in Fig. 22 and yield the displacement time history at R in the absence and presence of tunnels. Once again, we observe how the presence of shallow buried tunnels modifies the 'free-field' transient signals by introducing reverberations in the original recording that last well over $10.0\,\text{sec}$, and at the same changes the maximum signal amplitude. We note in passing that the displacement time histories produced by the FDM in Fig. 22(a) at the deposit's surface are virtually indistinguishable from those produced by the hybrid FDM-BEM technique when cavities are absent in the 'BEM box'.

6.6 Response of the Metro tunnels in the 'BEM' box to the 4/7/1978 M 5.1 aftershock

In this final set of results, the seismic signal used as input is the July 4, 1978 M 5.1 aftershock (Petrovski and Naumovski 1979, Skarlatoudis *et al*. 2012) of the June 1978 M 6.5 earthquake sequence that caused major damage in the city centre of Thessaloniki, Greece. This aftershock was recorded at station SEK resting on outcrop rock at the northern end of the N-S cross-section of Fig. 2, close to station OBS. In order to use this record as input excitation, the original recording was (i) baseline corrected, (ii) band-pass filtered at corner frequencies of 0.5 Hz and 10 Hz, (iii) rotated from the original direction to a direction corresponding to the N-S cross-section so as to simulate transverse SH- motion and (iv) corrected by removing the free surface effect so as to recover the incidence wave field. Fig. 23 shows both the acceleration time history of this event and the corresponding Fourier spectrum, where it is observed that the frequency content lies primarily within the $0-5$ Hz range. The displacement time history at the ‘BEM box’ interface was computed using double integration, as dictated by the complex convolution operation between the FDM synthetic transfer functions from the previous analysis using the Gabor pulse input with the event acceleration given in Fig. 23(a). Finally, the FFT of the displacement time history at the interface serves as input to the 'BEM-box' itself.

Table 2 Error (as %) in the displacement amplitude at two observation points *A*, *R* on the free surface as obtained by the BEM and the FEM for the Thessaloniki 4/7/1978 M 5.1 aftershock

Frequency	1.0 (Hz)	2.0 (Hz)	3.0 (Hz)	4.0 (Hz)	5.0 (Hz)
A(910 m, 26 m)	0.01	0.05	0.50	0.65	2.61
R(940 m, 28 m)	0.02	0.09	0.04	0.17	0.14

In order to show the generality of the present hybrid method, we replace the BEM solution by the finite element method (FEM). More specifically, we used the commercial program ANSYS (2009) and the corresponding FEM mesh comprises 3508 solid eight-node finite elements, resulting in 7320 nodal points. By way of comparison, the basic 'BEM-box' surface discretization scheme employed by the BEM throughout this work required 89 quadratic BE resulting in 179 nodal points (both meshes are shown in Fig. 24). In Table 2 we depict the displacement amplitude error (as a percentage) between the BEM and FEM results at surface observation points *A*(910,26) and *R*(940,28), for five discrete frequencies of 1; 2; 3; 4; 5 Hz. It can be observed that the maximum percent difference is 2.61% at *R*, the point close but not directly above the tunnels, and at the highest frequency value. This error was much smaller at other points that were examined along the free surface, indicating correct implementation of the hybrid method.

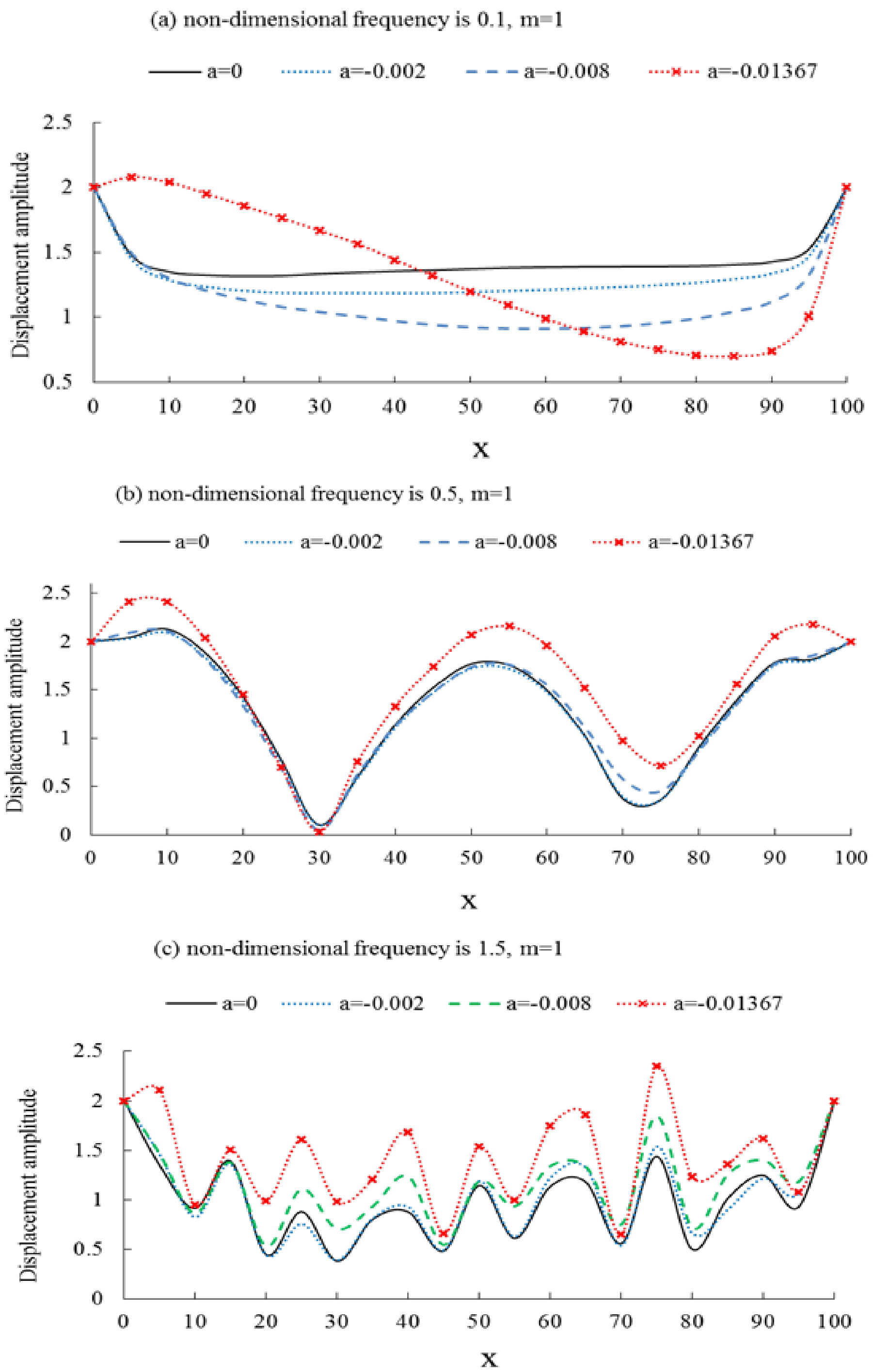

Fig. 18 Free surface displacement amplitude distribution for a quadratically inhomogeneous, isotropic geological finite region with tunnels embedded in the half-plane at different values of parameter *a* and for three dimensionless frequency values of: (a) $\Omega = 0.1$; (b) $\Omega = 0.5$ and (c) $\Omega = 1.5$

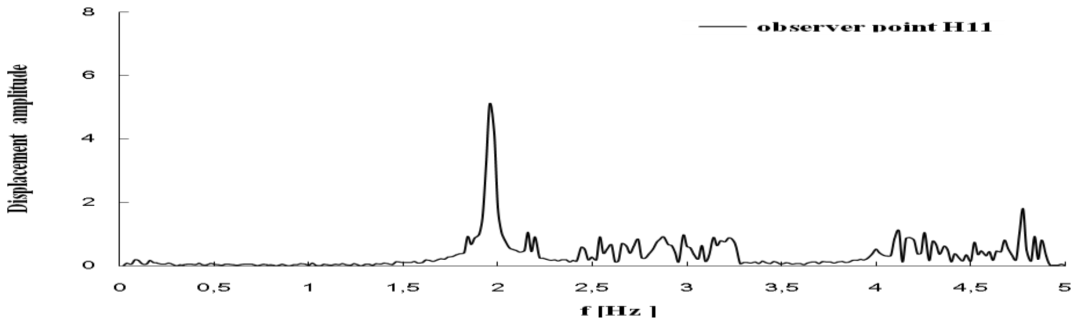

(a)

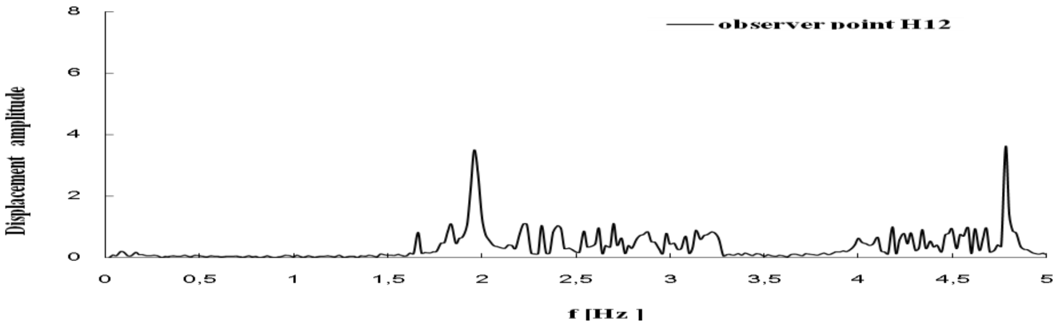

(b)

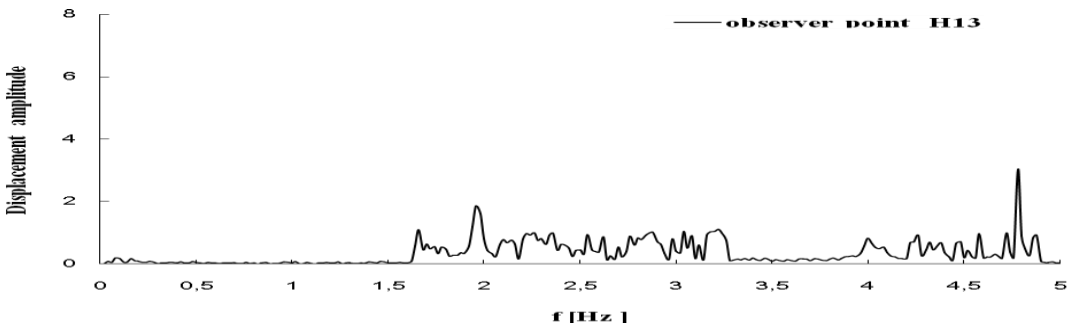

(c)

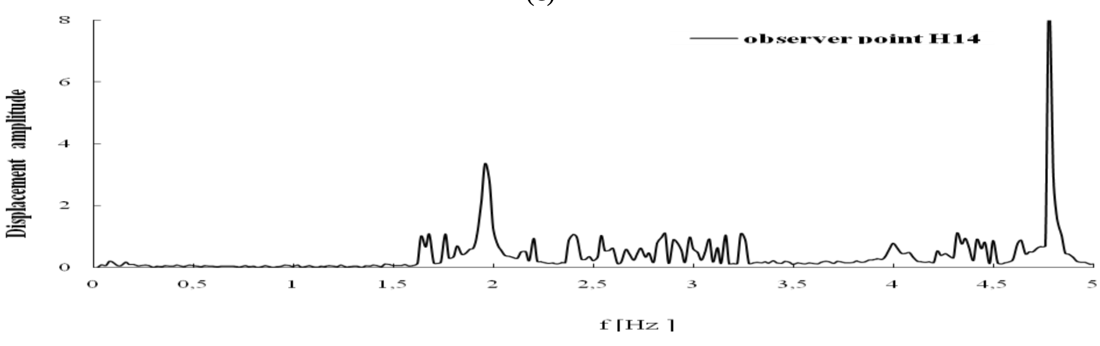

(d)

Fig. 19 Normalized displacement amplitude versus frequency at four points clockwise along the left Metro cavity perimeter for a Gabor pulse: (a) *H11*; (b) *H12*; (c) *H13* and (d) *H14*

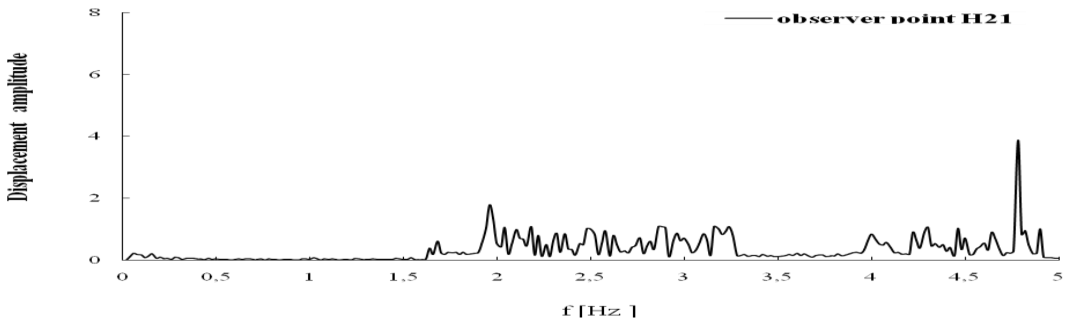

(a)

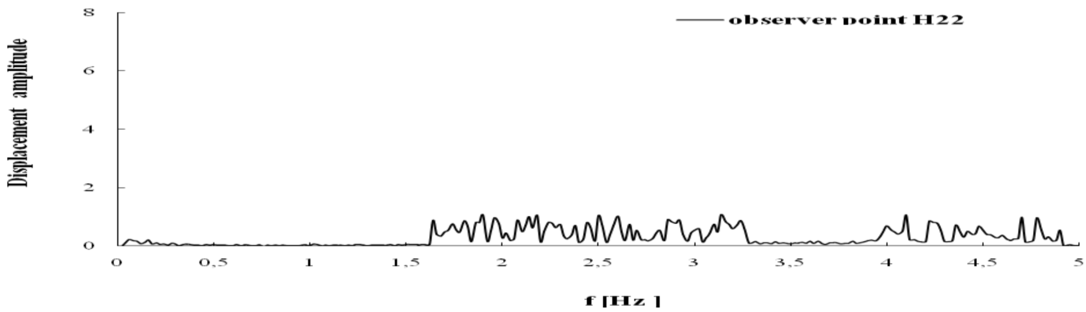

(b)

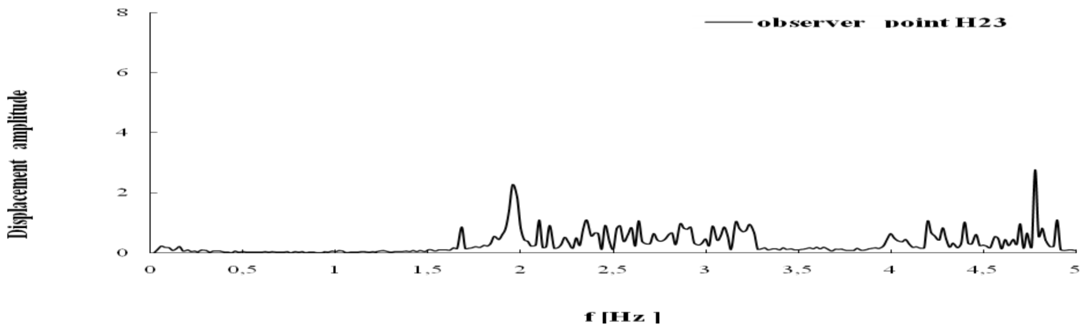

(c)

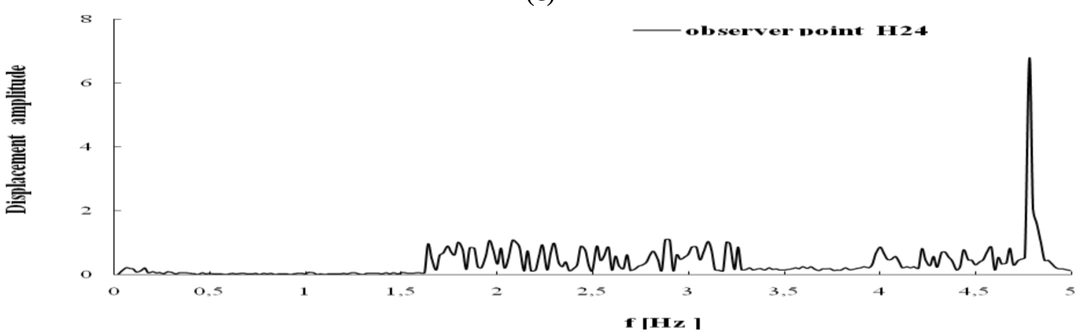

(d)

Fig. 20 Normalized displacement amplitude versus frequency at four points clockwise along the right Metro cavity perimeter for a Gabor pulse: (a) *H21*; (b) *H22*; (c) *H23*; (d) *H24*

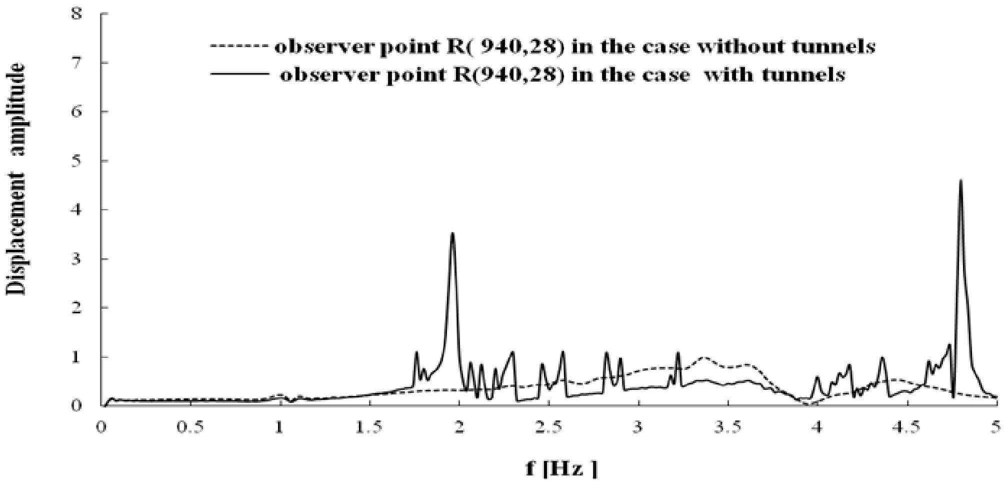

Fig. 21 Normalized frequency spectrum for the surface displacement at observation point *R* corresponding to the location of the Rotunda in the presence and absence of the Metro tunnels for a Gabor pulse

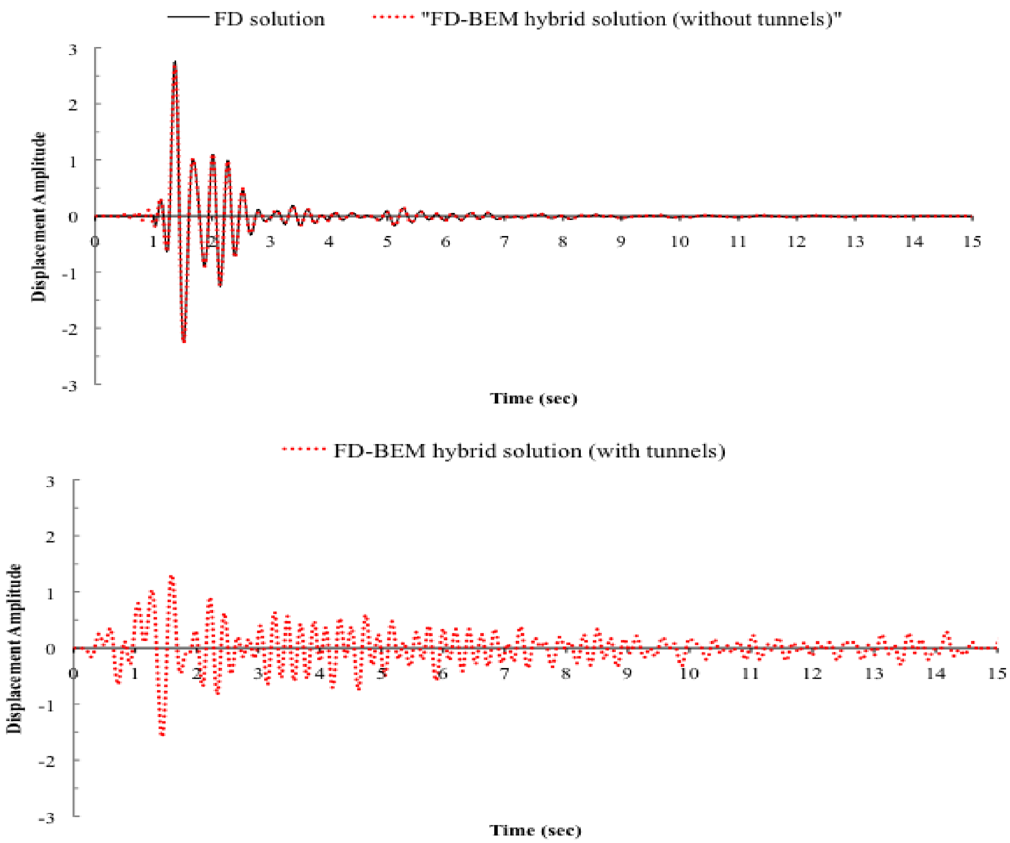

Fig. 22 Displacement time histories at observation point *R* corresponding to the location of the Rotunda monument for a Gabor pulse in the: (top) absence and (btm) presence of buried Metro tunnels

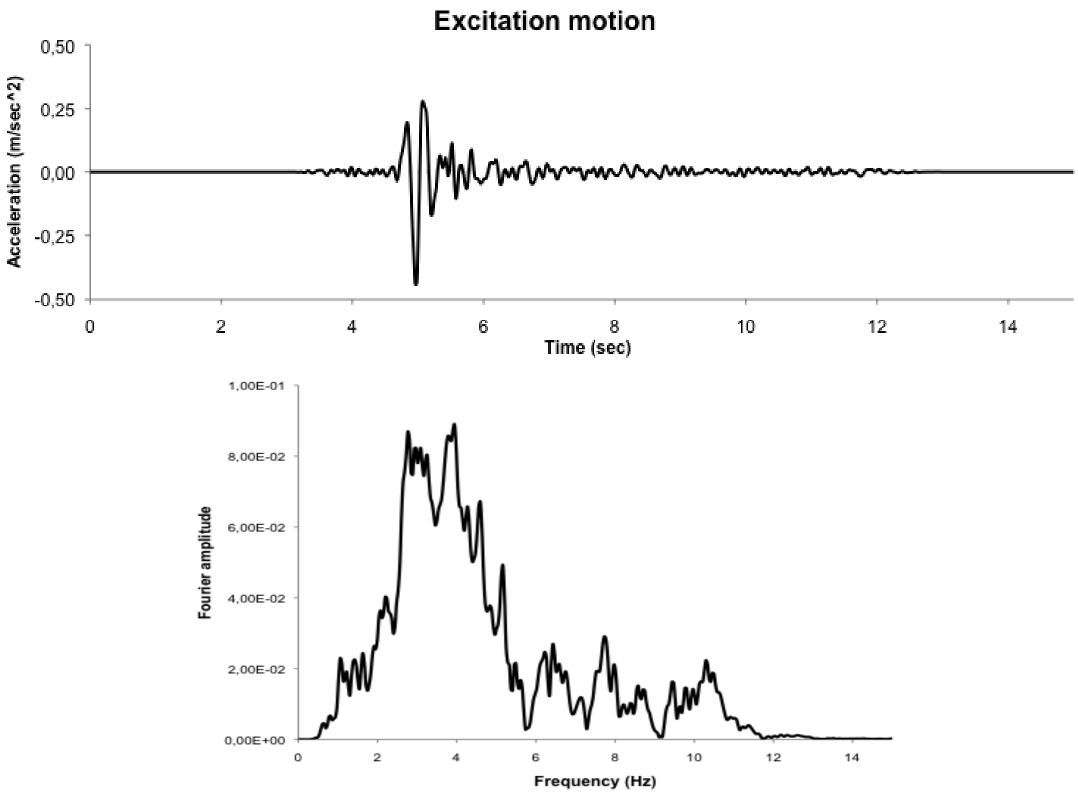

Fig. 23 The Thessaloniki 4/7/1978 M 5.1 aftershock of the Thessaloniki June 1978 earthquake sequence: (top) acceleration time history and (btm) corresponding Fourier spectrum

Next, Fig. 25 plots the surface displacement amplitudes at *A*, *R* as functions of frequency. We again observe the difference in the spectra between point *A* that is directly above the Metro tunnels and point *R* corresponding to the Rotunda monument location. Although in both cases there is a peak at around 2.7 Hz, this displacement peak is more pronounced in the former case, while in the latter case a secondary peak appears around 3.2 Hz. The results here are consistent with what was observed for the out-of-plane displacements in the case of the Gabor pulse given in the previously.

We then continue with the acceleration time histories at *R* that are plotted in Fig. 26(a) in the absence of tunnels (FDM solution only) and in Fig. 26(b) where tunnels are present (hybrid FDM-BEM). As with the Gabor pulse excitation case, the latter time history reverberates a little longer than the former one, but with less pronounced magnitude. The next two plot in Fig. 26 is for absolute acceleration response spectrum corresponding to the presence and absence of the tunnels in the soil deposit. These types of spectra could serve as a design tool for earthquake engineering purposes, as they clearly show that the presence of underground tunnels in the vicinity of the site in question is responsible for modifying the seismic input to above ground construction. Nevertheless, in order to definitely conclude how the presence of tunnels affects the seismically-induced input to nearby structures and what the engineering implications are, a detailed parametric study conforming with the seismic hazard characteristics of the Thessaloniki area is required, which is beyond the scope of the present work.

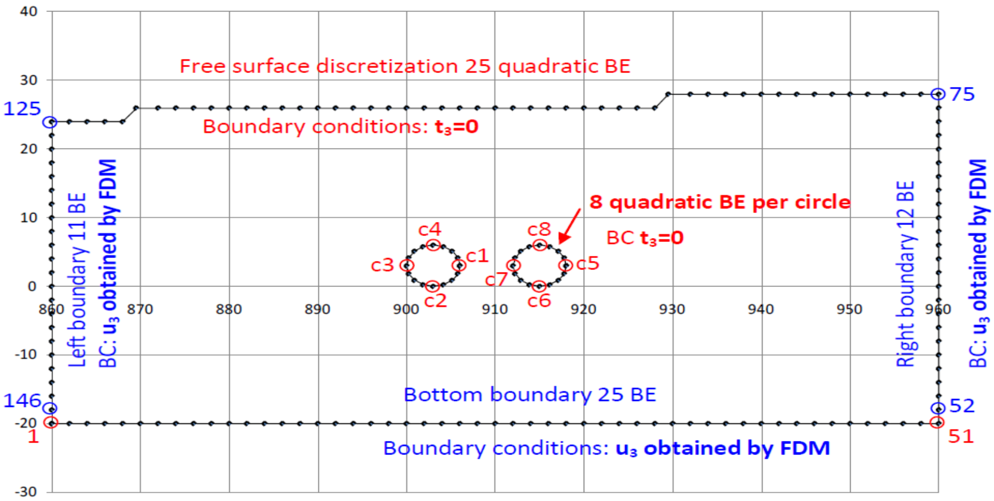

(a)

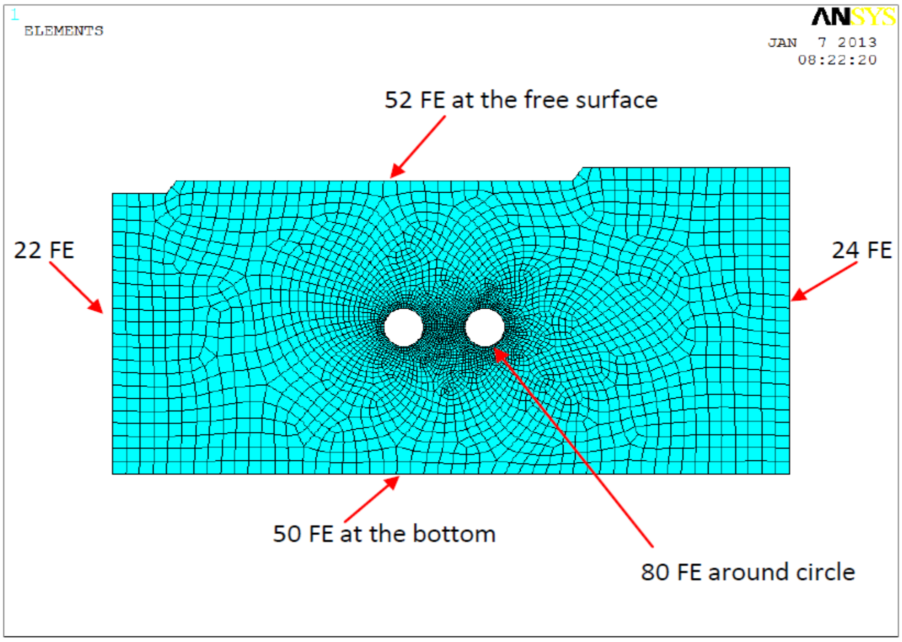

(b)

Fig. 24 Discretization of the local soil region with the Metro tunnels by the (a) BEM and (b) FEM with input provided by the FDM for the Thessaloniki 4/7/1978 M 5.1 aftershock

The final set of results have to do with the frequency dependence of the shear stresses σ_{23} that develop at the four observation points *H11- H14* along the perimeter of the left cavity (similar results were obtained by the BEM for the right cavity) for the Thessaloniki 1978 aftershock, see Fig. 27. We note here that higher values are recorded at observation points along the vertical faces, and especially on the vertical face opposite to the right cavity, at a frequency value of about 2.7 Hz. By way of contrast, the stress spectrum is less pronounced and rather diffused in the $2.5-3.5$ Hz range for the observation points at the top and bottom cavity faces, with the bottom face recording values that are about one-quarter less than the maximum ones.

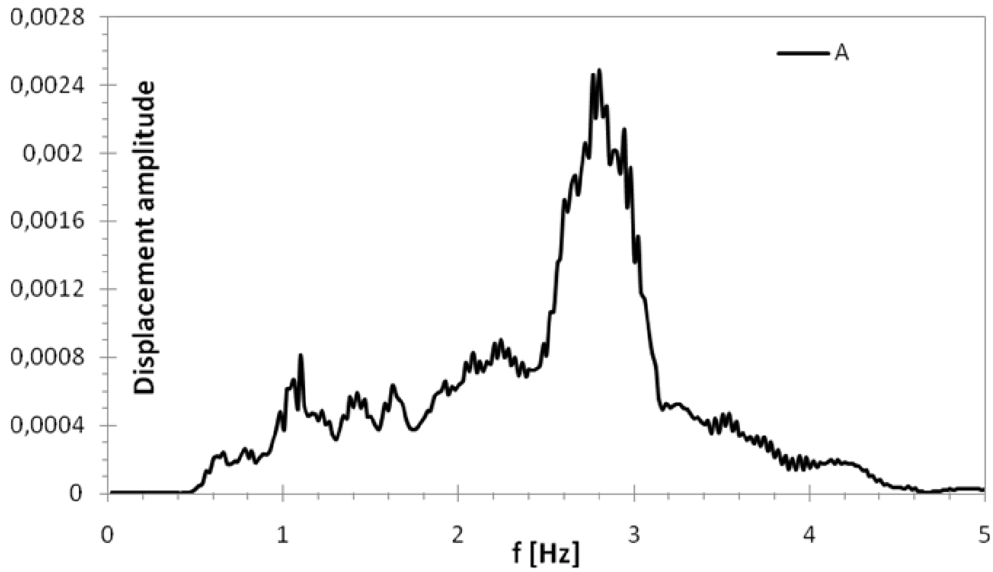

(a)

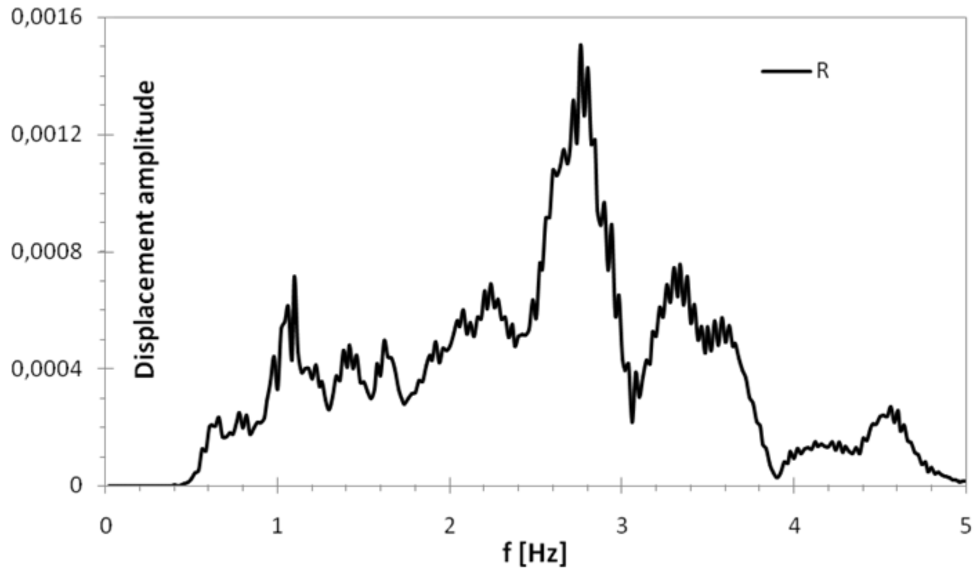

(b)

Fig. 25 Displacement amplitude $U_3 = U_z$ (in m) versus frequency at observation points (a) A and (b) R at the free surface for the Thessaloniki 4/7/1978 M 5.1 aftershock

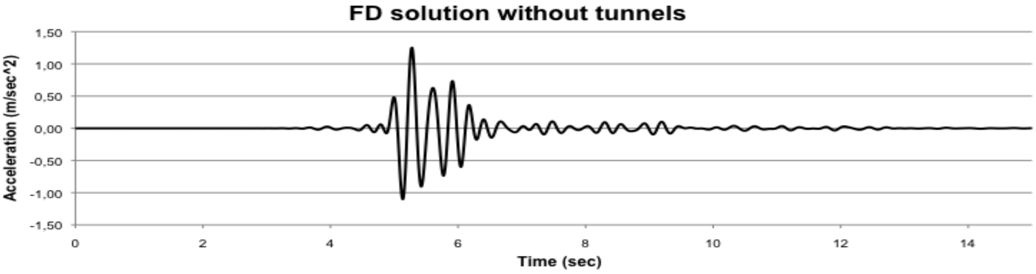

(a)

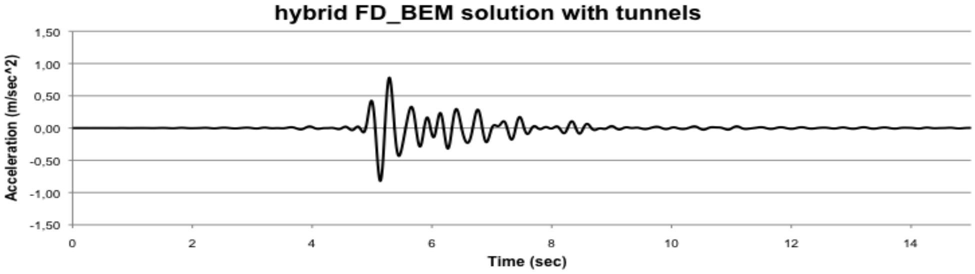

(b)

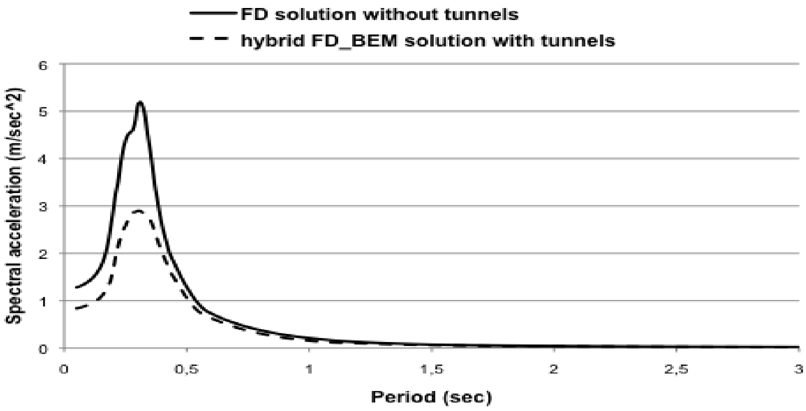

(c)

Fig. 26 Acceleration time histories for the (a) FDM and (b) hybrid FDM-BEM solutions at observation points *R* in the absence and presence of tunnels and (c) the corresponding absolute normalized response spectra for the Thessaloniki 4/7/1978 M 5.1 aftershock

7. Conclusions

An efficient BEM model for coupling with a pre-existing FDM model was developed in this work to solve complex, 2D finite geological regions excited by SH-waves. More specifically, the BEM model is based on both displacement and traction formulations that employ recently obtained fundamental solutions derived by use of the Radon transform for continuously inhomogeneous and anisotropic elastic media. For saturated soils, Bardet's model is introduced as

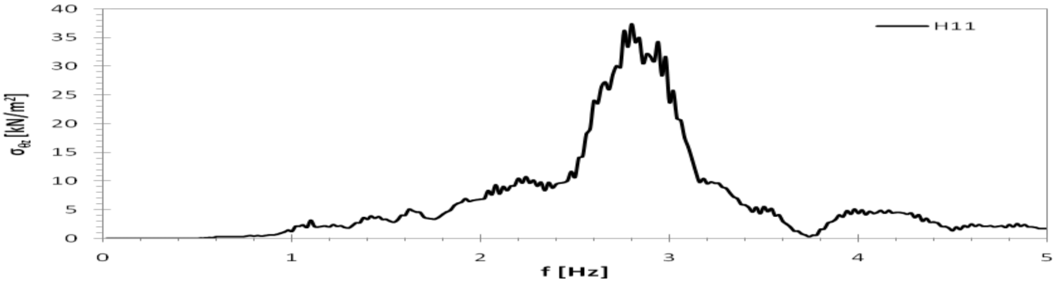

(a)

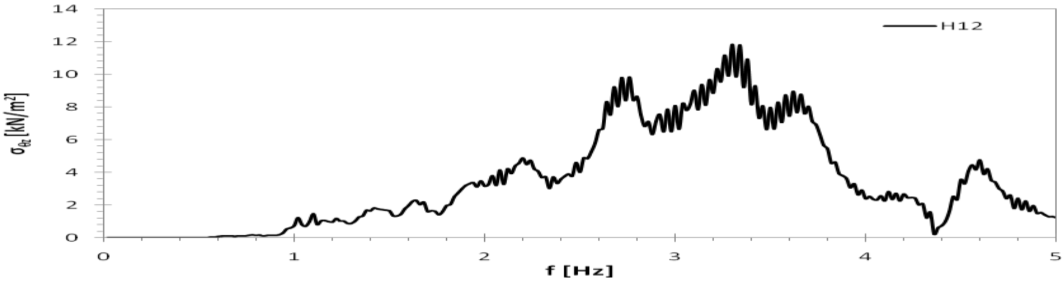

(b)

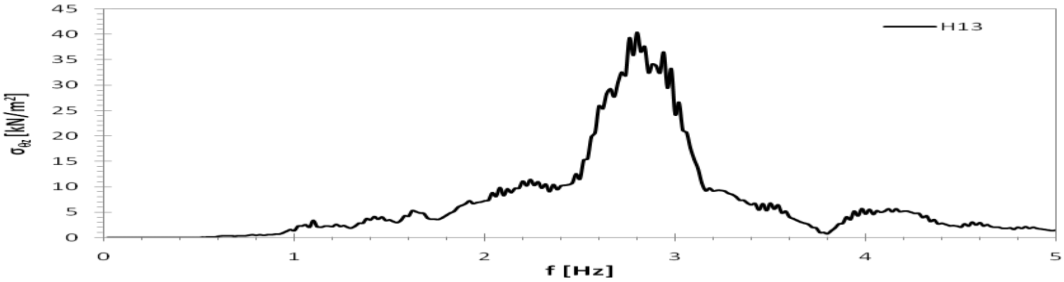

(c)

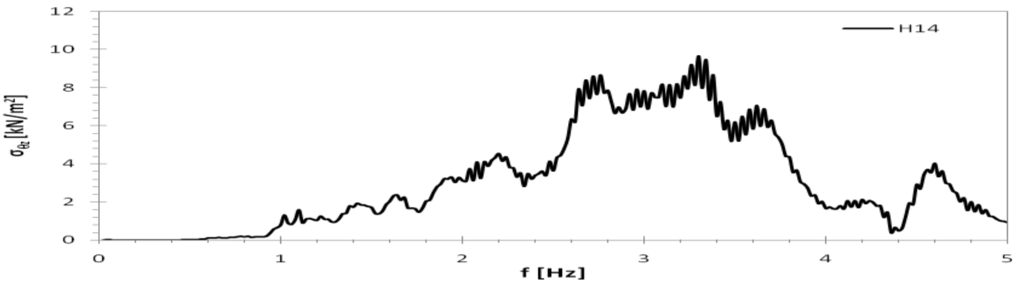

(d)

Fig. 27 Shear stress $\sigma_{23} = \sigma_{\Theta Z}$ (in kN/m^2) vs. frequency at observation points (a) H_{11}, (b) H_{12}, (c) H_{13} and (d) H_{12} *c-w* along the left cavity perimeter for the Thessaloniki 4/7/1978 M 5.1 aftershock

the computationally efficient viscoelastic isomorphism to Biot´s equations of dynamic poroelasticity, allowing wave field evaluations for an equivalent one-phase viscoelastic medium.

Thus, the BEM model is capable of representing complex material behavior, surface topography effects plus the presence of buried cylindrical cavities. Following accuracy and convergence tests on the BEM, numerical results were generated for a key cross-section of the Thessaloniki, Greece Metro construction project that includes the historical Roman monument known as the Rotunda complex. At first, the FDM was used to generate the wave field in the absence of the Metro tunnels, and this information was subsequently imparted to the localized 'BEM-box' region. For verification purposes, a dense FEM mesh replaced the aforementioned 'BEM-box' and yielded the same results as before. Finally, free surface displacement time histories, cavity perimeter stress time histories and acceleration spectra were computed for a wave pulse and for a recorded accelerogram from the Thessaloniki, Greece June 1978 M 6.5 earthquake sequence, both emanating from the bedrock interface. The signal variability observed locally due to the presence of buried tunnels has important design consequences for the built environment. It is also important in helping decide the exact placement of tunnels so as to minimize free surface vibration phenomena. Future improvements will included incorporation of geological discontinuities such as cracks, plus the modelling of P- and SV- waves.

Acknowledgement

Author PSD acknowledges support provided by the MC-IEF grant PIEF-GA-2010-270889, while authors GDM and TVR acknowledge support provided by Grant No. CLG-984136. Finally, we thank Prof. S. Parvanova of UACEG, Sofia, for her help with the FEM computations.

References

Ahmad, S., Leyte, F. and Rajapakse, R.K.N.D. (2001), “BEM analysis of two-dimensional elastodynamic problems of anisotropic solids”, *J. Eng. Mech. - ASCE*, **127**, 149-156.

Alterman, Z.S. and Karal, F.C. (1968), “Propagation of elastic waves in layered media by finite difference methods", *B. Seismol. Soc. Am.*, **58**, 367-398.

Alvarez-Rubio, S., Benito, J.J., Sánchez-Sesma, F.J. and Alarcon, E. (2005), “The use of direct boundary element method for gaining insight into complex seismic site response”, *Comput. Struct.*, **83**, 821-835.

ANSYS Release 10.0 (2009), *Structural mechanics package*, Canonsburg, Pennsylvania

Aznarez, J.J., Maezo, O. and Dominguez, J. (2006), “BE analysis of bottom sediments in dynamic fluid-structure interaction problems”, *Eng. Anal. Bound. Elem.*, **30**, 124-136.

Bardet, J.P. (1992), “A viscoelastic model for the dynamic behaviour of saturated poroelastic soils”, *Transac. ASME*, **59**, 128-135.

Bielak, J. and Christiano, P. (1984), “On the effective seismic input for nonlinear soil- structure-interaction systems“, *Earthq. Eng. Struct. Dyn.*, **12**, 107-119.

Bielak, J., Loukakis, K., Hisada, Y. and Yoshimura, C. (2003) “Domain reduction method for three-dimensional earthquake modelling in localized regions. Part I: Theory“, *B. Seismol. Soc. Am.*, **93**(2), 817-824.

Biot, M. (1956), “Theory of propagation of elastic waves in a fluid-saturated porous solid”, *J. Acoust. Soc. Am.*, **28**(4), 168-191

Bouchon, M. and Sánchez-Sesma, F.J. (2007), “Boundary integral equations and boundary elements methods in elastodynamics”, *Adv. Geophys.*, **48**, 157-189.

CEN (2004), *Eurocode 8: Design provisions of structures for earthquake resistance. Part 1: General rules, seismic actions and rules for buildings*, Final Draft pr EN1998-1, European Committee for Standardization, Brussels.

Christensen, R.M. (1971), *Theory of viscoelasticity: an introduction*, Academic Press, New York.

Denda, M., Wang, C.Y. and Yong, Y.K. (2003), "2D time-harmonic BEM for solids of general anisotropy with application to eigenvalue problems", *J. Sound Vib.*, **261**, 247-276.

Dineva, P. and Manolis, G.D. (2001), "Scattering of seismic waves by cracks in multi-layered geological regions: I. Mechanical model & II. Numerical results", *Soil Dyn. Earthq. Eng.*, **21**, 615-625 & 627-641.

Dineva, P., Manolis, G.D. and Rangelov, T.V. (2006), "Sub-surface crack in inhomogeneous half-plane: wave scattering phenomena by BEM", *Eng. Anal. Bound. Elem.*, **30**(5), 350-362.

Dineva, P., Rangelov, T.V. and Gross, D. (2005), "BEM for 2D steady-state problems in cracked anisotropic materials", *Eng. Anal. Bound. Elem.*, **29**, 689-698.

Dineva, P., Rangelov, T.V. and Manolis, G.D. (2007), "Elastic wave propagation in a class of cracked functionally graded materials by BEM", *Computat. Mech.*, **39**(3), 293-308.

Dravinski, M. and Niu, Y. (2002), "Three-dimensional time-harmonic Green's functions for a triclinic full-space using a symbolic computation system", *Int. J. Numer. Methods Eng.*, **53**, 455-472.

EERI (2003), "Preliminary observations on the August 14, 2003 Lefkada Island (Western Greece) Earthquake", Special Earthquake Report, http://www.eeri.org/.

Fäh, D. (1992), "A hybrid technique for the estimation of strong ground motion in sedimentary basins", PhD Thesis, ETH Nr. 9767, Swiss Federal Institute of Technology, Zurich, Switzerland.

Fäh, D., Suhadolc, P., Muller, S. and Panza, G.F. (1994), "A hybrid method for the estimation of ground motion in sedimentary basins: quantitative modelling for Mexico City", *B. Seismol. Soc. Am.*, **84**(2), 383-399.

Fäh, D., Suhadolc, P. and Panza, G.F. (1990), "Estimation of strong ground motion in laterally heterogeneous media: modal summation-finite differences", *Proceedings of the 9th European Conference on Earthquake Engineering*, Moscow, USSR, Vol. 4A, pp. 100-109.

Fäh, D., Suhadolc, P. and Panza, G.F. (1993), "Variability of seismic ground motion in complex media: the case of a sedimentary basin in the Friuli Italy area", *J. Appl. Geophys.*, **30**, 131-148.

Galis, M., Moczo, P. and Kristek, J. (2008), "A 3-D hybrid finite-difference-finite-element viscoelastic modelling of seismic wave motion", *Geophys. J. Int.*, **175**, 153-184.

Gatmiri, B. and Jabbari, E. (2005), "Time-domain Green's functions for unsaturated soils. Part I: Two-dimensional solution & Part II: Three-dimensional solution", *Int. J. Solids Struct.*, **42**(23), 5971-5990 & 5991-6002.

Gatmiri, B., Maghoul, P. and Arson, C. (2009), "Site-specific spectral response of seismic movement due to geometrical and geotechnical characteristics of sites", *Soil Dyn. Earthq. Eng.*, **29**, 51-70.

Goto, H., Ramírez-Guzmán, L. and Bielak, J. (2010), "Simulation of spontaneous rupture based on a combined boundary integral equation method and finite element method approach: SH and P-SV cases", *Geophys. J. Int.*, **183**(2), 975-1004.

Kattis, S.E., Beskos, D.E. and Cheng, A.H.D. (2003), "2D dynamic response of unlined and lined tunnels in poroelastic soil to harmonic body waves", *Earthq. Eng. Struct. Dyn.*, **32**, 97-110.

Kaynia, A.M. and Banerjee, P.K. (1992), "Fundamental solutions of Biot's equations of dynamic poroelasticity", *Int. J. Eng. Sci.*, **31**(5), 817-830.

Knopoff, R., Fredricks, R.F., Gangi, A.F. and Porter, L.D. (1957), "Surface amplitudes of reflected body waves", *Geophysics*, **22**(4), 842-847.

Kobayashi, S., Nishimura, N. and Kishima, T. (1986), *A BIE analysis of wave propagation in anisotropic media*, Boundary Elements VIII, Springer-Verlag, Berlin, 425-434.

Lee, V.W. (1977), "On deformation near circular underground cavity subjected to incident plane SH-waves", *Proceedings of Conference in Application of Computer Methods in Engineering*, University of South California, Los Angeles, pp. 951-962.

Lekhnitskii, S.G. (1963), *Theory of elasticity of an anisotropic elastic body*, Holden-Day, San Francisco.

Lin, C.H, Lee, V.W. and Trifunac, M.D. (2001), “On the Reflection of Elastic Waves in a Poroelastic Half-space Saturated with Non-viscous Fluid”, Report No. CE 01-04, Department of Civil Engineering, University of Southern California, Los Angeles.

Lin, C.H., Lee, V.W. and Trifunac, M.D. (2005), “The reflection of plane waves in a poroelastic half-space saturated with inviscid fluid”, *Soil Dyn. Earthq. Eng.*, **25**, 205-223.

Liu, H. and Zhang, C. (2003), “Internal stress calculation in 2D time domain BEM for wave propagation in anisotropic media”, *Int. J. Numer. Methods Biomed. Eng.*, (original title: Communications in Numerical Methods in Engineering), **19**(8), 637-643.

Luzón, F., Palencia, V.J., Morales, J., Sánchez-Sesma, F.J. and García, J.M. (2002), “Evaluation of site effects in sedimentary basins”, *Física de la Tierra*, **14**, 183-214.

Manolis, G.D. and Beskos, D.E. (1989), “Integral formulation and fundamental solutions of dynamic poroelasticity and thermoelasticity”, *Acta Mecanica*, **76**, 89-104.

Manolis, G.D., Dineva, P. and Rangelov, T. (2004), “Wave scattering by cracks in inhomogeneous continua using BEM”, *Int. J. Solids Struct.*, **41**(14), 3905-3927.

Manolis, G.D., Dineva, P. and Rangelov, T.V. (2012) “Dynamic fracture analysis of a smoothly inhomogeneous plane containing defects by BEM”, *Eng. Anal. Bound. Elem.*, **36**, 727-737.

Manolis, G.D., Rangelov, T.V. and Dineva, P. (2007), “Free-field wave solutions in a half-plane exhibiting a special-type of continuous inhomogeneity”, *Wave Motion*, **44**, 304-321.

Manolis, G.D., Rangelov, T.V. and Dineva, P. (2009), “Free-field dynamic response of an inhomogeneous half-space”, *Arch. Appl. Mech.*, **79**, 595-603.

Manolis, G.D. and Shaw, R.P. (1996), “Green’s function for the vector wave equation in a mildly heterogeneous continuum”, *Wave Motion*, **24**, 59-83.

Moczo, P. (1989), “Finite-difference technique for SH waves in 2-D media using irregular grids: application to the seismic response problem”, *Geophys.J. Int.*, **99**, 321-329.

Moczo, P. and Bard, P.Y. (1993), “Wave diffraction, amplification and differential motion near strong lateral discontinuities”, *B. Seismol. Soc. Am.*, **83**(1), 85-106.

Moczo P., Bystricky E., Kristek J., Carcione M. and Bouchon M. (1997), “Hybrid modelling of P-SV seismic motion at inhomogeneous viscoelastic topographic structures”, *B. Seismol. Soc. Am.*, **87**(5), 1305-1323.

Moczo, P., Kristek, J., Galis, M., Pazak, P. and Balazovjech, M. (2007), “The finite-difference and finite-element modeling of seismic wave propagation and earthquake motion”, *Acta Physica Slovaca*, **51**(2), 177-406.

Moczo, P., Labák, P., Kristek, J. and Hron, F. (1996), “Amplification and differential motion due to an antiplane 2D resonance in the sediment valleys embedded in a layer over the half-space”, *B. Seismol. Soc. Am.*, **86**, 1434-1446.

Morochnik, V. and Bardet, J.P. (1996), “Viscoelastic approximation of poroelastic media for wave scattering problems”, *Soil Dyn. Earthq. Eng.*, **15**, 337-346.

Oprsal, I., Matyska, C. and Irikura, K. (2009), “The source-box wave propagation hybrid methods: General formulation and implementation“, *Geophys. J. Int.*, **176**, 555-564.

Oprsal, I., Pakzad, M., Plicka, V. and Zahradnik, J. (1998), “Ground motion simulation by hybrid methods”, In: K. Irikura, K. Kudo, H. Okada, T. Sasatani (Ed.), The Effects of Surface Geology on Seismic Motion, *Proceedings of ESG’98*, Yokohama, Japan, Vol. 2, Balkema, Rotterdam, 955-960.

Oprsal, I., Plicka, V. and Zahradnik, J. (1998), “Kobe simulation by hybrid methods”, In: K. Irikura, K. Kudo, H. Okada, T. Sasatani (Ed.), The Effects of Surface Geology on Seismic Motion, *Proceedings of ESG’98*, Yokohama, Japan, Vol. 3, Balkema, Rotterdam, 1451-1456.

Oprsal, I. and Zahradnik, J. (2002), “Three-dimensional finite difference method and hybrid modeling of earthquake ground motion”, *J. Geophys. Res.*, **107**(B8), 16-29.

Petrovski, D. and Naumovski, N. (1979), *Part I-Analytical methods in processing of strong motion accelerograms*, Publication No. 66, Institute of Earthquake Engineering and Engineering Seismology, Skopje, F.Y.R. of Macedonia, pp.1-69.

Rangelov, T., Dineva, P. and Gross, D. (2003), "A hypersingular traction boundary integral equation method for stress intensity factor computation in a finite cracked body", *Eng. Anal. Bound. Elem.*, **27**(1), 9-21

Rangelov, T.V., Manolis, G.D. and Dineva, P. (2005), "Elastodynamic fundamental solutions for certain families of 2D inhomogeneous anisotropic domains: Basic derivations", *Eur. J. Mech. A-Solids*, **24**, 820-836.

Raptakis, D., Makra, K., Anastasiadis, A. and Pitilakis, K. (2004a), "Complex site effects in Thessaloniki (Greece): I. Soil structure and confrontation of observations with 1D analysis", *B. Earthq. Eng.*, **2**(3), 271-300.

Raptakis, D., Makra, K., Anastasiadis, A. and Pitilakis, K. (2004b), "Complex site effects in Thessaloniki (Greece): II. 2D SH modeling and engineering insights", *B. Earthq. Eng.*, **2**(3), 301-327.

Rizzo, F.J. and Shippy, D. (1970), "A method for stress determination in plane anisotropic elastic bodies", *J. Compos. Mater.*, **4**, 36-61.

Robertson, J.O.A. and Chapman, C.H. (2000), "An efficient method for calculating finite-difference seismograms after model alterations", *Geophysics*, **65**, 907-918.

Saez, A. and Domınguez, J. (1999), "BEM analysis of wave scattering in transversely isotropic solids", *Int. J. Numer. Methods Eng.*, **44**, 1283-1300.

Schanz, M. and Pryl, D. (2004), "Dynamic fundamental solutions for compressible and incompressible modelled poroelastic continua", *Int. J. Solids Struct.*, **41**, 4047-4073.

Skarlatoudis, A.A., Papazachos, C.B. and Theodoulidis, N. (2012), "Site-response study of Thessaloniki (Northern Greece) for the 4 July1978 M 5.1 aftershock of the June 1978 M 6.5 sequence using a 3D finite-difference approach", *B. Seismol. Soc. Am.*, **102**, 722-737.

Smerzini, C., Aviles, J., Paolucci, R. and Sánchez-Sesma, F.J. (2009), "Effect of underground cavities on surface earthquake ground motion under SH wave propagation", *Earthq. Eng. Struct. Dyn.*, **38**, 1441-1460.

Snyder, M.D. and Cruse, T.A. (1975), "Boundary integral analysis of anisotropic cracked plates", *Int. J. Fract. Mech.*, **11**, 315-328.

Vrettos, C. (1991), "In-plane vibrations of soil deposits with variable shear modulus. II: Line load", *Int. J. Numer. Anal. Methods Geomech.*, **14**, 649-662.

Wang, C.Y. and Achenbach, J.D. (1995), "Three-dimensional time-harmonic elastodynamic Green's functions for anisotropic solids", *Proceedings of the Royal Society of London A*, **449**, 441-458.

Wang, C.Y., Achenbach, J.D. and Hirose, S. (1996), "Two-dimensional time domain BEM for scattering of elastic waves in anisotropic solids", *Int. J. Solids Struct.*, **33**, 3843-3864.

Wuttke, F., Dineva, P.S. and Schanz, T. (2011), "Seismic wave propagation in laterally inhomogeneous geological region via a new hybrid approach", *J. Sound Vib.*, **330**, 664-684.

Zahradnik, J. and Moczo, P. (1996), "Hybrid seismic modelling based on discrete wave number and finite difference methods", *PAGEOPH*, **148**(1-2), 21-38.

Zhang, Ch. and Gross, D. (1998), *On wave propagation in elastic solids with cracks*, Computational Mechanics Publication, Southampton.

SA